Journal of Nanobiotechnology

RESEARCH

Open Access

Porphyromonas gingivalis extracellular vesicles exacerbated osteoporosis by disrupting osteoblast mitochondrial dynamics and inhibiting Cpt2-regulated fatty acid oxidation

Qiujing Qiu[1†], Xiaoyuan Yan[1†], Zeying Zhang[1], Xiyue Zhang[1], Jiawei Ma[1], Wenqing Gao[1], Na An[2*], Lihong Qiu[1*] and Jiajie Guo[1*]

Abstract

Background Recent studies have implicated periodontitis (PD) as a potential risk factor for osteoporosis; however, the precise mechanisms remain unclear. *Porphyromonas gingivalis* (*Pg*), a key pathogen associated with PD, can secrete extracellular vesicles (EVs). However, whether *Pg* EVs can be transported to the bone marrow and influence osteoporosis-related osteoblast differentiation warrants exploration. This study compares *Pg* EVs with EVs from *Porphyromonas endodontalis* (*Pe*), which is a less virulent congener but the evidence for its pathogenicity in PD is weak.

Results *Pg* EVs can be translocated into the marrow of mice and be internalized by osteoblasts through clathrin- and lipid raft-mediated endocytosis, thereby exacerbating osteoporosis. *Pg* EVs promote mitochondrial fission and inhibit mitochondrial fusion, leading to mitochondrial fragmentation, impaired mitochondrial activity and suppressed osteogenic differentiation. Furthermore, *Pg* EVs downregulate the protein level of carnitine palmitoyl transferase 2 (Cpt2) and inhibit fatty acid oxidation (FAO) by disrupting mitochondrial dynamics, which impairs osteoblast ATP production and exacerbates osteoporosis. The effects of *Pe* EVs are similar but weaker than those of *Pg* EVs.

Conclusions This study elucidates that *Pg* EVs exacerbate osteoporosis by disrupting osteoblast mitochondrial dynamics and suppressing Cpt2-regulated FAO. This study contributes to understanding of the etiological

[†]Qiujing Qiu and Xiaoyuan Yan have contributed equally to this work.

*Correspondence:
Na An
nan@cmu.edu.cn
Lihong Qiu
lhqiu@cmu.edu.cn
Jiajie Guo
guojiajie@cmu.edu.cn

Full list of author information is available at the end of the article

© The Author(s) 2025. **Open Access** This article is licensed under a Creative Commons Attribution-NonCommercial-NoDerivatives 4.0 International License, which permits any non-commercial use, sharing, distribution and reproduction in any medium or format, as long as you give appropriate credit to the original author(s) and the source, provide a link to the Creative Commons licence, and indicate if you modified the licensed material. You do not have permission under this licence to share adapted material derived from this article or parts of it. The images or other third party material in this article are included in the article's Creative Commons licence, unless indicated otherwise in a credit line to the material. If material is not included in the article's Creative Commons licence and your intended use is not permitted by statutory regulation or exceeds the permitted use, you will need to obtain permission directly from the copyright holder. To view a copy of this licence, visit http://creativecommons.org/licenses/by-nc-nd/4.0/.

mechanisms through which *Pg* contributes to the progression of osteoporosis and highlights the pivotal role of EVs in the association between periodontal disease and systemic diseases.

Keywords *Porphyromonas gingivalis*, Extracellular vesicles, Osteoblast, Mitochondrial dynamics, Carnitine palmitoyl transferase 2, Fatty acid oxidation

Graphical Abstract

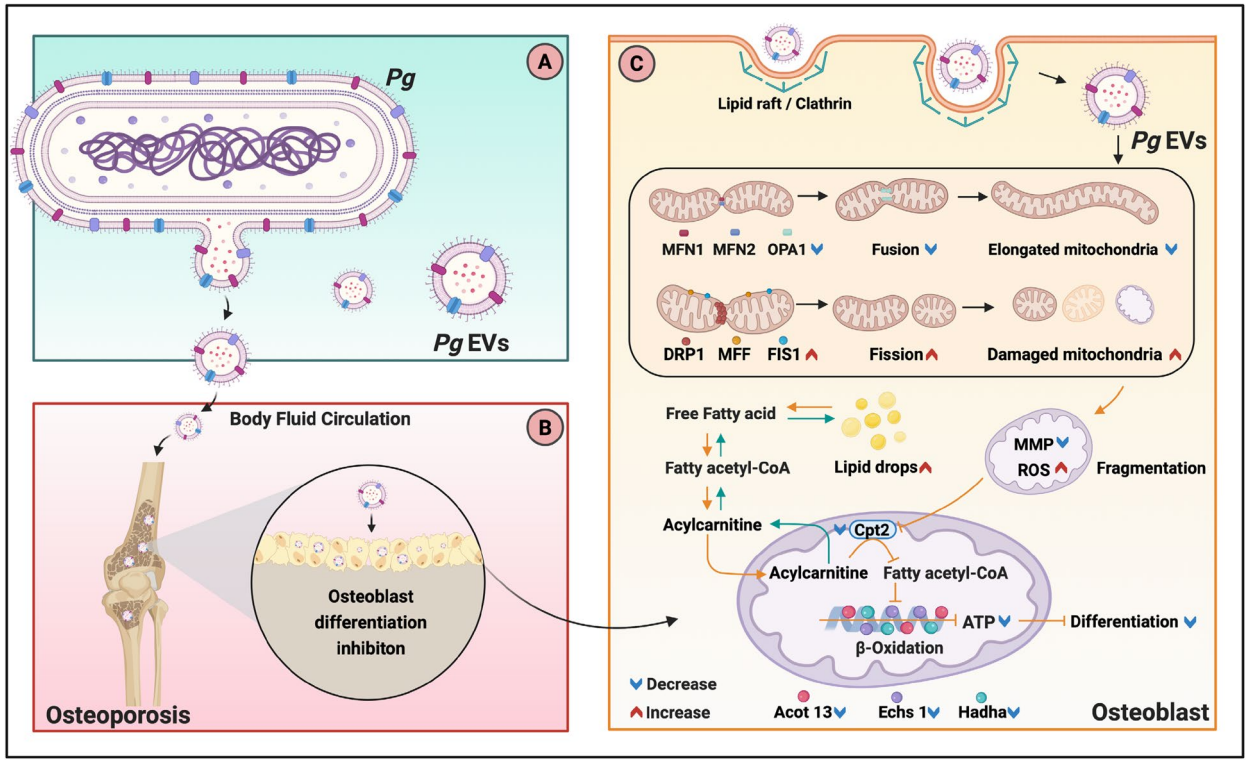

Background

Periodontitis (PD) is an inflammatory disease of the periodontium that is characterized by alveolar bone loss [1], while osteoporosis is a systemic skeletal disorder marked by reduced bone density and quality, affecting around 200 million people globally [2]. Emerging evidence suggests a link between PD and osteoporosis, with severe PD increasing osteoporosis risk by 1.38-fold, and up to 6.02-fold in populations with poor oral hygiene [3]. Experimental evidence has also shown that PD can exacerbate bone loss in osteoporotic rats [4–6]. These findings suggest that PD may be a risk factor for osteoporosis. *Porphyromonas gingivalis* (*Pg*), a black-pigmented, gram-negative, anaerobic bacterium, is one of the primary pathogens responsible for PD. Previous research has detected *Pg* 16S rDNA specifically in the blood of rats with ligature-induced osteoporosis, which suggests a relationship between *Pg* and osteoporosis [6]. However, to date, there have been no reports on how *Pg* affects osteoporosis.

Pg can secrete extracellular vesicles (EVs) [7]. EVs carry outer membrane proteins, periplasmic substances, lipopolysaccharides, and nucleic acids. Studies revealed that inhibiting EVs released from *Pg* alleviated the inhibition of bone regeneration in extraction sockets under *Pg* imbalance, suggesting that EVs serve as a critical virulence group contributing to *Pg*-induced bone destruction [8]. EVs can be transported to distant organs to trigger tissue damage and immune responses [9–11]. For instance, *Pg* EVs can be transported to the liver and alter blood glucose metabolism [7]. EVs from other oral pathogens can cross the blood–brain barrier to deliver RNA and trigger neuroinflammation [12, 13], or accumulate in bone marrow and exacerbate systemic bone loss [14]. Therefore, whether *Pg* EVs can be transported to the bone marrow via bodily fluids and influence the development of osteoporosis through direct interaction with bone-associated cells warrants exploration, but no relevant studies have been reported.

Osteoporosis results from excessive bone resorption and insufficient bone formation [15]. Osteoblasts, derived from mesenchymal stem cells, which can synthesize type I collagen, induce matrix mineralization, and construct the bone microarchitecture [16], play a critical

role in bone formation [17]. Mitochondria, as the main cellular energy supply centers, significantly influence osteogenic differentiation [18]. Mitochondria constantly undergo dynamic fusion (merging into one) or fission (splitting into two) to maintain the stability of the mitochondrial network and make adaptive changes in the cellular energy supply [19]. Mitochondrial fusion facilitates the interconnection of electron transport chain complexes, favoring oxidative phosphorylation (OXPHOS) and fatty acid oxidation (FAO) for energy production, whereas mitochondrial fission leads to swelling of the mitochondrial cristae, which separate the electron transport chain complexes from each other and shift cellular metabolism toward glycolysis [20]. Hence, alterations in mitochondrial dynamics can lead to the reprogramming of cellular metabolism. Therefore, this study aimed to further investigate whether *Pg* EVs can disrupt osteoblast differentiation by influencing mitochondrial dynamics.

Fatty acid oxidation (FAO) is a major pathway for cellular energy production [21], which serves as the major energy pathway for osteoblasts, particularly during mineralization [22]. In addition, osteoblasts rely on FAO to maintain the energy supply during the mineralization and maturation phases [23, 24]. Carnitine palmitoyl transferase 2 (Cpt2) is located in the inner membrane of mitochondria and is mainly responsible for converting acylcarnitine into acyl-CoA [25]. Acyl-CoA subsequently participates in β-oxidation. Inhibition of Cpt2 expression reduces β-oxidation and leads to decreased whole-body bone mass in mice [26, 27]. An intact mitochondrial morphology provides attachment sites for Cpt2 and ensures the necessary catalytic conditions for FAO. Therefore, whether *Pg* EVs interfere with mitochondrial dynamics in osteoblasts, leading to the reduction of Cpt2 protein level and subsequently affecting FAO and osteoblast differentiation, remains unclear.

This study compared EVs derived from *Pg* with those from *Porphyromonas endodontalis* (*Pe*), a species within the same genus exhibiting relatively lower virulence [28, 29]. Both *Pg* EVs and *Pe* EVs could translocate to the bone marrow in mice and be internalized by osteoblasts, exacerbating osteoporosis through the inhibition of osteogenic differentiation. Mechanistically, *Pg* EVs and *Pe* EVs promoted mitochondrial fission and inhibited fusion, leading to mitochondrial fragmentation and reduced Cpt2 levels. Furthermore, Cpt2 inhibition impeded the entry of free fatty acids into mitochondria, suppressed FAO and reduced lipid droplets (LDs) degradation, ultimately inhibiting osteoblast differentiation through decreased ATP production. These findings reveal a pathogenic pathway by which *Pg* EVs aggravate osteoporosis through impairing mitochondrial dynamics and FAO, providing novel experimental evidence for a deeper understanding of the biological mechanisms underlying the impact of PD on osteoporosis.

Materials and methods

EV extraction and characterization

P. endodontalis (*Pe*; ATCC 35406) and *P. gingivalis* (*Pg*; ATCC 33277) were cultured in brain heart infusion broth (Solarbio, Beijing, China; cat# LA0360) at 37 °C under anaerobic conditions. The culture medium was supplemented with 0.5% yeast extract (Thermo Fisher Scientific, Massachusetts, USA; cat# LP0021B), 10 μg/mL hemin (RYON, Shanghai, China; cat# 16,009–13-5), and 1 μg/mL vitamin K1 (MoFoKangYaoYe, Neijing, China). Bacterial morphology was observed by scanning electron microscopy (SEM; SU-3500, HITACHI, Tokyo, Japan) and transmission electron microscopy (TEM; H-7650, HITACHI, Tokyo, Japan).

EVs were isolated according to a protocol we described previously [9]. EVs were collected and resuspended in PBS and then stored at −80 °C. The protein concentration of the EVs was determined with a Bradford assay kit (Beyotime, Jiangsu, China; cat# P0006C). The EV size distribution was analyzed by using a Zetasizer nano ZSP (Malvern Panalytical, England). TEM was used to observe negatively stained EVs. Bacterial lysates and EVs (2 μg) were separated by 10% SDS–polyacrylamide gel electrophoresis (PAGE) and stained with a rapid silver staining kit (Beyotime, Jiangsu, China; cat# P0017S). The peptides carried by the EVs were analyzed using a Q Exactive Orbitrap mass spectrometer (Thermo), with detection performed by LC-BIO Co., Ltd. (Hangzhou, China). The identification of EV marker proteins was performed using Western blotting (WB), with the relevant antibodies listed in Supplementary Table S1.

Cell culture and differentiation

The mouse preosteoblast cell line MC3T3-E1 was purchased from Procell (Wuhan, China; cat# CL-0378) and cultured in a 37 °C incubator with 5% CO_2. Primary calvarial osteoblasts were isolated from 3-day-old mice. The proliferation medium, which consisted of α-MEM (Procell; cat# 184 PM150210), was supplemented with 10% fetal bovine serum (FBS; Procell; cat# 164,210–50) and 1% penicillin/streptomycin (HyClone, UT, USA; cat# SV30010). The proliferation medium was supplemented with ascorbic acid (50 mg/mL, Sigma–Aldrich, MO, USA; cat# 50–81-7) and β-glycerophosphate (5 mM, Sigma; cat# 154,804–51) to generate the osteogenic differentiation medium. To investigate the effects of EVs on osteoblast differentiation, the differentiation medium containing EVs was replaced every 2 days until the designated treatment time was reached.

Intracellular localization of EVs by fluorescence microscopy

EVs (1 μg/μL) were incubated with DiL dye (10 μM, Beyotime; cat# C1036) for 30 min at 37 °C. Unbound dye was removed by washing 3 times with total exosome isolation reagent (Thermo; cat# 4,478,359). MC3T3-E1 cells or primary calvarial osteoblasts were stimulated with DiL-labeled EVs for 4 h. The cells were fixed with 4% paraformaldehyde for 20 min, after which the cytoskeleton was labeled with ActinTracker Green-488 (1% v/v, Beyotime; cat# C2201SS) for 30 min at 37 °C. Nuclei were labeled with DAPI (1:1000, Solarbio; cat# C0060) for 10 min at room temperature (RT). Images were acquired with a confocal laser scanning microscope (Olympus, FV3000, Japan).

To validate the intracellular internalization of EVs, the cells were pretreated with pitstop 2 (Aladdin; cat# P414453) or methyl-β-cyclodextrin (MβCD; Aladdin; cat# M102038) for 30 min. The subsequent methodology follows the same procedure as described in the preceding section.

ALP staining and activity assay

For ALP staining, the cells were fixed with 4% paraformaldehyde and stained with an alkaline phosphatase staining kit (Beyotime; cat# C3250S). For ALP activity detection, the cells were lysed by using Western and IP cell lysis buffer (Beyotime; cat# P0013J) with the aid of a sonicator. The cell lysate was then incubated with a chromogenic substrate (Beyotime; cat# P0321S) at 37 °C for 10 min, after which a stop solution was added to the mixture. The absorbance at 450 nm was measured by using a microplate reader (Tecan, Infinite® 200 PRO, Switzerland).

Alizarin red S staining and quantification

For alizarin red staining, the cells were fixed with the fixative provided in the osteoblast mineralization nodule staining kit (Beyotime; cat# C0148S) and then stained with alizarin red. After the staining plates were dried, 1 mL of 10% hexadecyl-pyridinium chloride solution (Aladdin, Shanghai, China; cat# 6004–24-6) was added to dissolve the stained mineralized nodules for 15 min. The dissolved mineral mixture was collected, and the absorbance at 540 nm was measured by using a microplate reader (Tecan).

ATP and free fatty acid (FFA) concentration assays

ATP assays were performed using lysates prepared from cell samples or isolated mouse serum samples. In accordance with the instructions of the ATP assay kit (Beyotime; cat# S0026), ATP assay working solution was added to the prepared cell lysate or serum, and the RLU value was measured with a microplate reader (Tecan).

For the intracellular FFA content assay, FFA were extracted from the cells by using BeyoLysis™ Buffer A from the Amplex Red Free Fatty Acid Assay Kit (Beyotime; cat# S0215S). Mouse serum samples were isolated. The enzyme mixture and FFA assay working solution were added to the cell extract or serum, and the FFA content was analyzed by measuring the absorbance value at 570 nm with a microplate reader (Tecan).

Mitochondrial morphology observation by TEM

MC3T3-E1 cells were cultured for 3 days in differentiation medium containing EVs. The cells were subsequently fixed with fresh electron microscopy fixative (Servicebio, Wuhan, China; cat# G1102) and stored at 4 °C overnight. The cells were then rinsed with 0.1 M sodium cacodylate buffer and fixed in 1% osmium tetroxide for 1.5 h at RT. Following dehydration in a graded ethanol series, the cells were embedded in Spurr resin (Polysciences, PA, USA; cat# 01916–1). Ultrathin sections were cut and stained with uranyl acetate and lead citrate. Finally, the intracellular mitochondrial morphology was observed using TEM (HITACHI).

Mitochondrial extraction

MC3T3-E1 cells were cultured in differentiation medium for 5 days, and intact mitochondria were extracted with a Cellular Mitochondrial Isolation Kit (Beyotime; cat# C3601). The extracted mitochondria were resuspended in the storage solution provided within the kit and quickly transferred to −80 °C for storage. A Bradford kit was used to determine the protein concentration of the mitochondria.

siRNA construction and knockdown

Drp1 siRNA (si-Drp1), Fis1 siRNA (si-Fis1) and negative control siRNA (si-NC) were designed and synthesized by Sangon Biotech Co., Ltd. (Shanghai, China). The specific sequences of si-Drp1 and si-Fis1 are shown in Table S2. INTERFERin® (PolyPlus, Illkirch, France; cat# 101,000,028) was used as the transfection reagent. Next, 10 nM si-Drp1, si-Fis1, or si-NC was diluted in 200 μL of fresh α-MEM without FBS. After vortexing for 10 s, 6 μL of INTERFERin® was added and incubated for 10 min at RT; then, the transfection mixture was added to 800 μL of fresh medium to establish a 1 mL transfection system. For transfection, MC3T3-E1 cells were incubated in medium containing transfection solution for 6 h. The medium was then replaced with fresh medium containing EVs or PBS, and the cells were incubated for the indicated times.

Overexpression plasmids

The Opa1 overexpression plasmid (OE-Opa1), Mfn1 overexpression plasmid (OE-Mfn1), Cpt2 overexpression

plasmid (OE-Cpt2), and negative control overexpression plasmid (OE-NC) were designed and synthesized by Shanghai Genechem Co., Ltd. (Shanghai, China). The overexpression plasmid vectors are shown in Fig. S1. jetPRIME® (PolyPlus; cat# 101,000,027) was used as the transfection reagent. One microgram of OE-Opa1, OE-Mfn1, OE-Cpt2, or OE-NC plasmid was diluted in 200 μL of transfection buffer. After vortexing for 10 s, 2 μL of jetPRIME® reagent was added, and the mixture was incubated at RT for 10 min. The transfection mixture was then added to 800 μL of fresh medium to prepare a 1 mL transfection system. For transfection, MC3T3-E1 cells were cultured in medium containing the transfection mixture for 6 h, after which the medium was replaced with fresh medium containing EVs or PBS, and the cells were cultured until the designated time point.

Fluorescence staining

To evaluate mitochondrial morphology, the cells were incubated with MitoTracker Green (100 nM, Beyotime; cat# C1048) or MitoTracker Red CMXRos (100 nM, Beyotime; cat# C1049B) for 30 min at 37 °C. If LD staining was also performed, the cells were incubated with BODIPY 500/510 C1 or C12 (10 μM, Beyotime; cat# C2055-1 mg) for 30 min at 37 °C. Images were acquired with a confocal microscope (Olympus). Mitochondrial network analysis was then performed on at least 3 intact cells per group by using MiNA 3.0, which is a Fiji plugin for mitochondrial morphology analysis.

For mitochondrial ROS detection, the cells were incubated with MitoSOX Red mitochondrial superoxide indicator (10 μM, MedChemExpress, New Jersey, USA; cat# 1,003,197–00-9) for 30 min at 37 °C, followed by incubation with Hoechst 33,342 (Beyotime; cat# C1017) for 10 min at 37 °C to stain the nuclei.

To determine the mitochondrial membrane potential (MMP), the cells were incubated with JC-1 (20 μg/mL, AAT Bioquest, California, USA; cat# 3520–43-2) for 30 min at 37 °C to label the mitochondrial membrane. After staining, the medium was replaced with fresh medium, and fluorescence was observed with a confocal laser scanning microscope (Olympus).

Western blotting

Cell lysates were prepared by using Western and IP cell lysis buffers (Beyotime) and were separated by SDS–polyacrylamide gel electrophoresis (PAGE). The proteins were then transferred to PVDF membranes (Merck; cat# IPVH00011). The membranes were blocked with QuickBlock™ Western blocking buffer (Beyotime; cat# P0252) for 15 min and then incubated overnight at 4 °C with primary antibodies diluted in QuickBlock™ Western antibody dilution buffer (Beyotime; cat# P0239). The membranes were washed with Western washing buffer (Beyotime; cat# P0023C3) and incubated with fluorescent secondary antibodies diluted in QuickBlock™ Western secondary antibody dilution buffer (Beyotime; cat# P0023D) for 1 h at RT. All the antibodies used are listed in Table S1. The stained protein bands were visualized by using an Odyssey® DLx imaging system (LI-COR, NE, USA).

Real-time quantitative PCR

Total cellular RNA was extracted with the Eastep® Super Total RNA Extraction Kit (Promega, Beijing, China; cat# LS1040). cDNA was synthesized by using the PrimeScript Reverse Transcription Kit (Takara, Shiga, Japan; cat# RR036A). qPCR mixtures were prepared by using qPCR SYBR Premix Ex Taq™ (Takara; cat# RR820A), and qPCR was performed on an ABI 7500 system (Applied Biosystems, CA, USA) to detect the mRNA expression of target genes. The relative mRNA levels were calculated via the 2^(-ΔΔCt) method and were normalized to β-actin expression levels. The sequences of primers used are listed in Table S3.

FAO assay

The original culture medium was removed, and the cells were washed three times with PBS for 3 min each time. The instructions for obtaining the cell lysate were followed, the protein concentration was measured, and FAO activity was determined using a Fatty Acid Oxidation (FAO) Colorimetric Assay Kit (Elabscience; cat# E-BC-K784-M).

Animal experiments

Animal studies were approved by the Institutional Animal Care and Use Committee of China Medical University (CMU2023680, CMU20241480). Female C57BL/6 J mice were purchased from SPF Biological Technology Co., Ltd. (Beijing, China). The mice were randomly assigned to groups (5 mice/cage) and housed in a specific-pathogen-free (SPF)-grade environment with controlled humidity and temperature on a 12-h light/12-h dark cycle.

To investigate EV transport in vivo, EVs (1 μg/μL) were incubated with DiR dye (5 μM; Yeasen, Shanghai, China; cat# 40757ES25) at 37 °C in the dark for 30 min. After washing, the EVs were resuspended in PBS. Ten-week-old female mice received intraperitoneal injections of 100 μL of PBS or DiR-labeled EVs (0.2 μg/μL). One and three hours postinjection, the mice were euthanized, and their hearts, lungs, livers, kidneys, spleens, and lower limb bones were harvested. The fluorescence intensity and distribution of DiR were observed with an AniView100 multimodal in vivo imaging system (Boluteng Biological Technology Co., Ltd., Guangzhou, China).

To investigate the effects of EVs on osteoporosis in mice, 10-week-old female mice were subjected to bilateral OVX to establish an osteoporosis model. Sham-operated mice were subjected to only the ovarian exteriorization procedure and were then sutured. In accordance with the resource equation method [30], 14–24 mice were used as experimental subjects in this study. A total of 20 mice were used in this study, with 5 mice in each group. Two weeks post-surgery, the experimental mice received intraperitoneal injections of 100 μL of EVs (0.2 μg/mL) for 4 weeks. The control and sham-operated mice received an equivalent volume of PBS. On day 3 after the last injection, the mice were euthanized, and bone and blood samples were collected. Mouse femurs were fixed with 4% paraformaldehyde at 4 °C for 48 h prior to analysis.

To overexpress Cpt2 in osteoblasts, we constructed an AAV serotype 9 vector (GeneChem, Shanghai, China). The Cpt2 sequence was subsequently cloned and inserted into the GV584 vector with the vector elements in the order of mRUNX2p-EGFP-FT2A-NM_009949.3-3flag-SV40 PolyA to construct an adeno-associated virus (AAV) for Cpt2 overexpression (AAV-Cpt2 and AAV-NC). In accordance with the resource equation method [30], 16–26 mice were used in this experiment. In practice, a total of 30 mice were used, with 5 mice in each group. As described previously, an osteoporosis mouse model was established. One week post-surgery, 5 μL of AAV-Cpt2 or AAV-NC (1E + 11 vg/mL) was injected into both knee joint cavities of the mice. One week after AAV injection, the mice were injected with PBS or EVs as described above. Three days after the last injection, the mice were euthanized, and liver, bone, and blood samples were collected as described previously.

Micro-CT analysis

Femurs were scanned by using a micro-CT system (Skyscan 1276, Bruker, MA, USA) at a working voltage of 55 kV and a working current of 72 μA, with an isotropic voxel size of 4 μm. The acquired trabecular and cortical bone images were reconstructed in 3D with CTvox software. CTAn software was used to analyze the bone volume (BV), tissue volume (TV), and trabecular number (Tb.N) of the trabecular bone.

Histological staining

Mouse bones were decalcified with 10% EDTA, paraffin-embedded, and sectioned. For hematoxylin–eosin (HE) staining, the sections were deparaffinized, rehydrated through a graded alcohol series, stained with hematoxylin (Servicebio; cat# G1004) for 10 min at RT, rinsed 3 times in water, treated with 1% (v/v) acid alcohol for 10 min, rinsed 3 times in water, and stained with eosin for 5 min, followed by a 3-min water rinse. The sections were then dehydrated and mounted with neutral balsam (Solarbio; cat# G8590).

For ALP staining of bone, the sections were deparaffinized and rehydrated as described above. The working solution was prepared with the Alkaline Phosphatase Staining Kit (Beyotime), and the sections were incubated with the ALP staining working solution overnight at 37 °C. The sections were rinsed with PBS and mounted with anti-fluorescence quenching mounting medium (Beyotime; cat# P0126-5 ml).

For immunohistochemical staining, the sections were deparaffinized and rehydrated as described above, and antigen retrieval was performed with pepsin (MXB Biotechnologies, Fuzhou, China; cat# DIG-3009). The sections were blocked with goat serum (BOSTER, Wuhan, China; cat# AR0009) to reduce nonspecific binding. The antibodies were diluted in PBS and incubated with the tissue sections overnight at 4 °C. A list of all the antibodies used is provided in Table S2. Color development was performed by using a DAB detection kit (Gene Tech, Wuhan, China; cat# GK600705). Nuclei were counterstained with hematoxylin (Servicebio), and the sections were rinsed with tap water, dehydrated, and mounted with neutral balsam.

For immunofluorescence staining of bone, decalcified bone and liver samples were embedded in optimal cutting temperature compound and sectioned at a thickness of 10 μm with a CM1950 cryostat (Leica, Nussloch, Germany). After the sections were allowed to stand at RT for 30 min, they were fixed in acetone at 4 °C for 5–10 min, followed by heat-induced antigen retrieval. The bone sections were incubated in blocking buffer containing 10% goat serum (BOSTER) and 0.3% Triton X-100 for 90 min at RT. DAPI (1:1000, Solarbio) was diluted in blocking buffer, and the sections were incubated at 4 °C for 48 h.

Statistical analysis

The data are presented as the means ± standard deviations (SDs). Comparisons between two independent groups were performed via Student's t test. One-way analysis of variance (ANOVA) followed by Dunnett's test was used for multiple group comparisons. The significance level for all analyses was set at $\alpha = 0.05$.

Results

Pg EVs and Pe EVs can be transported to the mouse bone marrow cavity and internalized by osteoblasts

We first characterized the bacteria and EVs. SEM revealed spherical protrusions on the cell membranes of both *Pg* and *Pe* (Fig. 1A). TEM revealed outer membrane blebbing, which formed spherical vesicular structures in both *Pg* and *Pe* (Fig. 1B). EVs were extracted, and TEM revealed that the EVs were unilamellar vesicular structures with a relatively uniform size (Fig. 1C). The

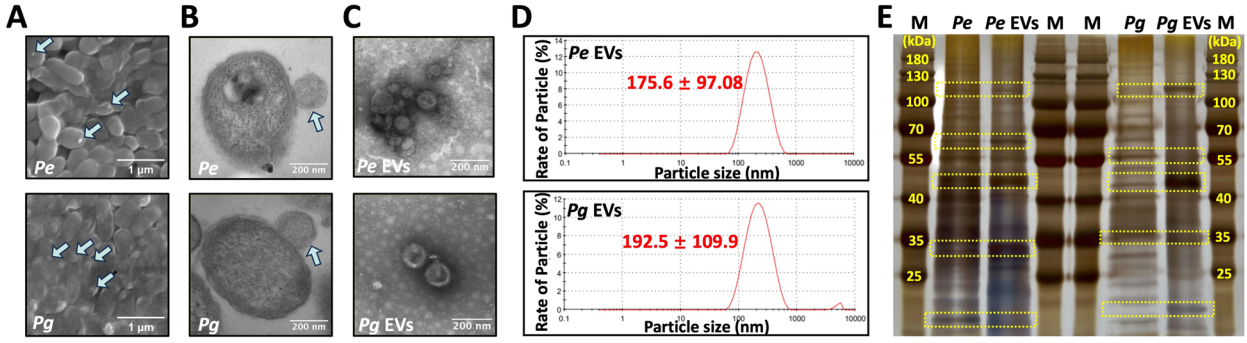

F

Pe EVs					*Pg* EVs				
	Description	MW [kDa]	Score Sequest HT	Accession		Description	MW [kDa]	Score Sequest HT	Accession
1	Glyceraldehyde-3-phosphate dehydrogenase	35.925	14.9722321	C3JA17	1	NAD-specific glutamate dehydrogenase	49.167	188.9100708	Q7MXJ7
2	Glutamate dehydrogenase	51.415	11.68862677	C3J7X5	2	RagA protein	112.305	137.9700521	P0C934
3	Propionyl-CoA carboxylase beta chain	56.233	11.45024192	C3J7Y9	3	Lipoprotein RagB	56.435	109.52956	F5H948
4	Chaperonin GroEL	58.262	7.712147951	C3J9K4	4	Minor fimbrium subunit Mfa1 C-terminal domain-containing protein	52.741	65.93525338	Q7MTR3
5	Gamma-aminobutyrate metabolism dehydratase/isomerase	56.76	7.584802151	C3J8J3	5	Glyceraldehyde-3-phosphate dehydrogenase	35.992	51.27234197	Q7MT61
6	Multifunctional fusion protein	50.551	3.743257642	C3JBB0	6	Gingipain R1	185.556	39.36521387	Q7MTE2
7	2,3-bisphosphoglycerate-dependent phosphoglycerate mutase	28.388	3.245693922	C3JBJ0	7	Ferritin	18.516	26.42198908	P59915
8	Urocanate hydratas	72.775	2.715704441	C3JCY3	8	Gingipain R2	80.916	26.10511017	P95493
9	DNA-directed RNA polymerase subunit beta	142.217	2.679619074	C3JC66	9	Hemagglutinin A	233.243	25.95871687	Q7MWD1
10	Methylmalonyl-CoA mutase	79.312	2.661329985	C3JCG0	10	4-hydroxybutyryl-CoA dehydratase	54	24.08132911	F5HE54
11	Fructose-1,6-bisphosphate aldolase, class II	36.313	2.003604412	C3JAQ9	11	Glucose-6-phosphate isomerase	48.937	20.16856468	Q7MV80
12	Peptidase family M13	76.957	1.93698287	C3J9F9	12	Peptidase, M24 family	66.54	19.82521641	P42375
13	Outer membrane protein, OMP85 family	102.269	1.78166914	C3J845	13	Peptidylarginine deiminase	61.69	18.51935303	Q9RQJ2
14	L-glutamate gamma-semialdehyde dehydrogenase	59.806	1.690278769	C3J9L0	14	Chaperonin GroEL	58.057	12.04316461	F5HE64
15	Enolase	45.802	0	C3JBK5	15	DNA protection during starvation protein	17.853	8.568704367	P0C935

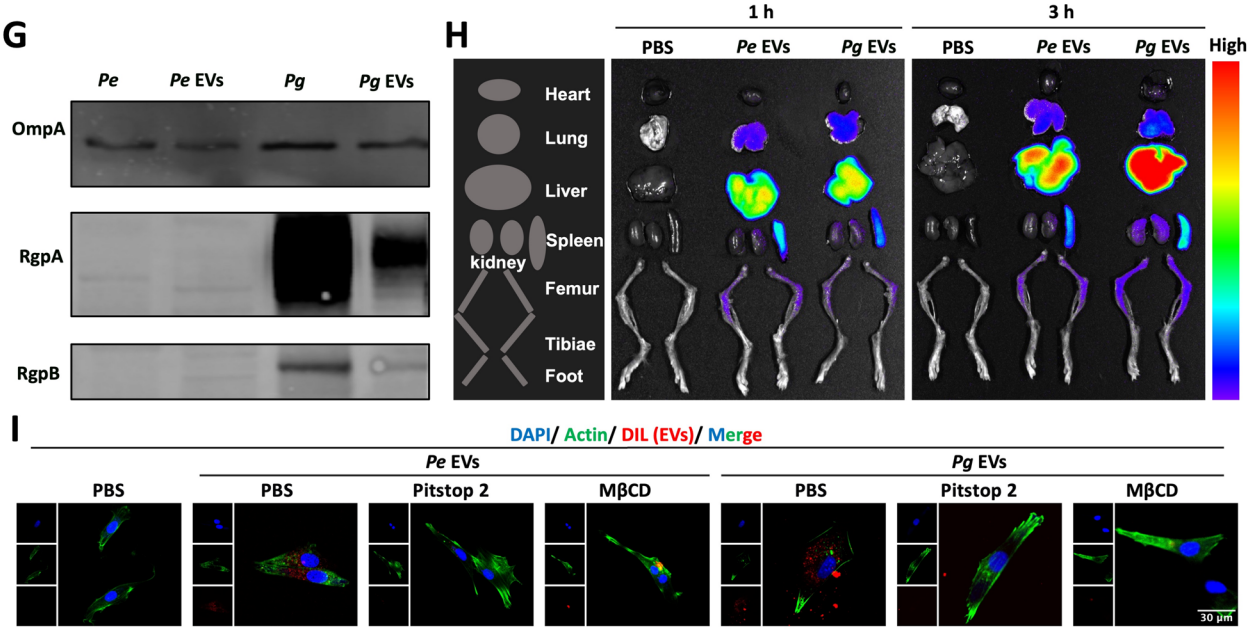

Fig. 1 (See legend on next page.)

(See figure on previous page.)

Fig. 1 Characterization of *Pg* EVs and *Pe* EVs and their transport in mice. (**A**) The surface morphology of *Pg* and *Pe* was examined by SEM. (**B**) EV budding from *Pg* and *Pe* was examined by TEM. (**C**) The ultrastructures of EVs were examined by TEM. (**D**) NTA of the EV particle size distribution. (**E**) Silver staining was used to compare the protein contents of EVs and their parental bacteria. The yellow box indicates proteins found in both EVs and their parental bacteria. (**F**) Mass spectrometry analysis of EVs components and listing the top 15 proteins ranked by Score Sequest HT. (**G**) Detection of EV marker proteins using WB. (**H**) DiR-labeled EV tracking in mice. (**I**) MC3T3-E1 cells were pretreated with pitstop 2 (30 μM) or MβCD (10 μM) for 30 min, followed by incubation with DiL-labeled (red fluorescence) EVs for 4 h. The actin cytoskeleton was labeled with Actin-tracker (green fluorescence), and the nuclei were labeled with DAPI (blue fluorescence)

average diameters of *Pg*-EVs and *Pe*-EVs were 192.5 nm and 175.6 nm, respectively (Fig. 1D). Multiple protein bands in the EVs corresponding to those in the bacterial cells (yellow box, Fig. 1E). Mass spectrometric analysis of EVs revealed that *Pe* EVs matched 23 peptides, identifying a total of 17 proteins, while *Pg* EVs matched 211 peptides, identifying a total of 51 proteins. Both *Pe* EVs and *Pg* EVs carried proteins such as Glutamate dehydrogenase, Glyceraldehyde-3-phosphate dehydrogenase and Chaperonin GroEL, which were closely associated with bacterial nutrient metabolism and the folding and activation of key proteins. But *Pg* EVs were enriched specifically for Gingipain R1 (RgpA) and Gingipain R2 (RgpB) (Fig. 1F). We further validated the expression of EV marker proteins. Both *Pe* EVs and *Pg* EVs expressed outer membrane protein A (OmpA), while RgpA and RgpB were specifically expressed in *Pg* EVs (Fig. 1G). Following intraperitoneal injection, DiR-labeled EVs were transported into the bone marrow cavity and other organs within 1 h, and their accumulation was enhanced after 3 h (Fig. 1H). Pitstop 2 and MβCD are inhibitors of clathrin-mediated endocytosis and lipid raft-dependent endocytosis, respectively. Both Pitstop 2 and MβCD inhibited the endocytic efficiency of *Pg*-EVs and *Pe*-EVs by osteoblasts to varying degrees, which indicated that *Pg*-EVs and *Pe*-EVs were internalized into osteoblasts via clathrin- and lipid raft-mediated endocytic pathways (Fig. 1I). These results demonstrated that both *Pg* and *Pe* were able to release EVs, which were transported into the bone marrow cavity and taken up by osteoblasts.

Pg EVs and Pe EVs inhibited osteoblast differentiation and aggravated osteoporosis

To further investigate the effects of *Pg* EVs and *Pe* EVs on osteoporosis, We established an osteoporosis mouse model and injected EVs intraperitoneally. Trabecular bone density decreased in the OVX-PBS group compared with the sham group, which confirmed the successful establishment of the osteoporosis model (Fig. 2A-D). EVs further decreased the density of bone trabeculae (Fig. 2A), bone volume (Fig. 2B), bone surface area (Fig. 2C), and number of trabeculae (Fig. 2D) in osteoporotic mice. Groups treated with EVs showed further reductions in the number of trabeculae in osteoporotic mice, accompanied by decreased levels of the osteogenic marker proteins collagen type I (Col-1) and osteopontin (OPN) and decreased ALP activity (Fig. 2E). In vitro, EVs inhibited ALP activity and mineralized nodule in a dose-dependent manner (Fig. 2F–K). For the subsequent in vitro experiments, a concentration of 1 μg/mL EVs was used. The PCR results revealed that *Pg* EVs and *Pe* EVs significantly inhibited the mRNA expression of the osteogenic differentiation marker genes Runx2, OSX, OCN, BSP, ALP and OPN (Fig. 2L–Q). These results suggest that *Pg* EVs and *Pe* EVs can aggravate bone loss in osteoporotic mice by inhibiting osteoblast differentiation.

Pg EVs and Pe EVs inhibited osteoblast differentiation by impairing mitochondrial activity

Mitochondria are critical organelles for cellular energy production, so we investigated the effects of EVs on osteoblast mitochondria. After MC3T3-E1 cells were treated with EVs for 24 h, the red fluorescence of MitoSOX Red-labeled mitochondrial ROS was significantly increased (Fig. 3A), and flow cytometry assays further verified this trend (Fig. 3B). EVs caused a decrease in the MMP (Fig. 3C, D). Immunohistochemistry revealed a further reduction in mitochondrial flux in bone from osteoporotic mice treated with EVs (Fig. 3E). These results demonstrated that *Pg* EVs and *Pe* EVs inhibited osteoblast mitochondrial activity.

Next, we investigated whether the addition of exogenous mitochondria could rescue the inhibition of mitochondrial activity mediated by EVs. We extracted intact mitochondria from MC3T3-E1 cells and verified their successful extraction via WB (Fig. 3F, G). Exogenous mitochondria at concentrations less than 1 μg/mL had no significant effect on cell viability (Fig. S2). The extracted exogenous mitochondria labeled with MitoTracker Green were taken up by MC3T3-E1 cells and integrated with the recipient cell mitochondria labeled with MitoTracker Red (Fig. 3H). The addition of exogenous mitochondria partially suppressed mitochondrial ROS (Fig. 3I, J), restored the MMP changes (Fig. 3K, L) and reversed ALP activity (Fig. 3M, N) mediated by EVs. Moreover, the expression levels of RUNX2 and OSX recovered (Fig. 3O–Q). These results indicated that the addition of exogenous mitochondria rescued the mitochondrial damage mediated by *Pg* EVs and *Pe* EVs and restored osteoblast differentiation.

Pg EVs and Pe EVs disrupted mitochondrial dynamics in osteoblasts

To further investigate the mechanism by which EVs impair mitochondrial activity, we examined osteoblasts

treated with EVs via TEM. EV-treated cells exhibited mitochondrial swelling and a decrease in the abundance of cristae, accompanied by an increase in the number of short spherical mitochondria, indicating that mitochondrial morphology was altered (Fig. 4A). Flow cytometry analysis revealed a decrease in mitochondrial abundance in osteoblasts stimulated with EVs (Fig. 4B). Mito-tracker staining revealed that EVs caused a shift from a network of interconnected elongated mitochondria to short and isolated fragments around the nucleus, with a reduction in mitochondrial branch length and footprint size (Fig. 4C–E). Similar mitochondrial fragmentation was also observed in mouse primary calvarial osteoblasts treated with EVs (Fig. S3). These phenomena suggested that the balance of mitochondrial dynamics, i.e., fusion and fission, was disrupted by EVs. EVs further upregulated the expression of the mitochondrial fission regulatory proteins Drp1, Fis1, and Mff and downregulated the expression of the mitochondrial fusion regulatory proteins Mfn1, Mfn2, and Opa1, with *Pg* EVs exhibiting a more pronounced effect than *Pe* EVs (Fig. 4F–L). In addition, *Pg* EVs and *Pe* EVs promoted the mRNA and protein expression of the mitophagy marker proteins Pink1 (PTEN-induced putative kinase 1) and Parkin (parkin RBR E3 ubiquitin protein ligase) (Fig. S4). Compared with the OVX-PBS group, the groups treated with EVs showed further increases in the expression of Drp1 and Fis1 and inhibition of the expression of Mfn1 and Opa1 in femur sections (Fig. 4M–P). These results revealed that *Pg* EVs and *Pe* EVs interfered with mitochondrial dynamics in osteoblasts by promoting mitochondrial fission and inhibiting mitochondrial fusion, which results in the fragmentation of mitochondria.

Pg EVs and Pe EVs impaired mitochondrial activity and inhibited osteoblast differentiation by disrupting mitochondrial dynamics

To further confirm whether EVs impair mitochondrial activity by disrupting mitochondrial dynamics, we constructed Mfn1 and Opa1 overexpression plasmids and siRNAs for Drp1 and Fis1 knockdown to investigate whether modulating mitochondrial dynamics could rescue mitochondrial activity. First, we verified the successful overexpression of Mfn1 and Opa1 (Fig. S5A–D). Compared with the NC group, the group subjected to co-overexpression of Mfn1 and Opa1 showed significantly increased mitochondrial length and footprint size in MC3T3-E1 cells after treatment with EVs (Fig. 5A–C), and the increase in mitochondrial ROS levels (Fig. 5D, E) and the decrease in the MMP (Fig. 5F, G) induced by EVs was partially alleviated. Moreover, overexpression of Mfn1 and Opa1 partially reversed the inhibition of ALP activity in osteoblasts mediated by EVs (Fig. 5H, I) and increased the expression of Mfn1, Opa1, Col-1, Runx2, and OSX (Fig. 5J–O). Similar results were obtained by simultaneously knocking down the mitochondrial fission genes Drp1 and Fis1. We verified the successful transfection of si-Drp1 and si-Fis1 (Fig. S6A–D). Under EV treatment, when the expression of Drp1 and Fis1 was inhibited, the average mitochondrial length and footprint size increased (Fig. S7A–C), the level of mitochondrial ROS decreased (Fig. S8A, B), the MMP increased (Fig. S9A, B), the ALP activity (Fig. S10A, B) and the expression of osteogenic differentiation marker proteins (Fig. S11A–G) increased. The above results indicated that upregulation of mitochondrial fusion or downregulation of mitochondrial fission could restore mitochondrial morphology and attenuate the inhibition of mitochondrial activity caused by *Pg* EVs and *Pe* EVs, ultimately rescuing the ability of osteoblasts to differentiate.

Pg EVs and Pe EVs inhibited Cpt2 expression, FFA oxidation, and ATP production in osteoblasts

Mitochondrial dynamics can modulate the rate of mitochondrial lipid catabolism. LDs can be catabolized into FFAs. Long-chain FFAs are activated to form acyl-CoA in the cytoplasm. Carnitine palmitoyl transferase 1 (Cpt1) and Cpt2 are key enzymes that regulate FFA entry into mitochondria and are located on the outer and inner mitochondrial membranes, respectively. Acyl-CoA is converted into acylcarnitine by Cpt1 for entry into mitochondria. Acylcarnitine is further catalyzed by Cpt2 to form acyl-CoA, which participates in subsequent β-oxidation and produces ATP. After EV infection, Cpt2 deficiency impairs FFA oxidation capacity; this inhibits the catabolism of LDs into FFAs, thereby preventing lipotoxicity-induced apoptosis and leading to increased intracellular LD abundance (Fig. 6A). EVs reduced ATP production in osteoblasts (Fig. 6B) and inhibited the gene expression of the mitochondrial respiratory chain proteins NADH Dehydrogenase Subunit 3 (Nd3) and NADH Dehydrogenase Subunit 4L (Nd4L) (Fig. S12A, B). Treatment with EVs also promoted the expression of the glycolysis rate-limiting enzymes hexokinase 2 (Hk2), pyruvate dehydrogenase kinase 1 (Pdk1) and phosphofructokinase-muscle (PFKM) (Fig. S12C–E). EVs also suppressed intracellular FFA levels (Fig. 6C) and FAO activity in osteoblasts (Fig. 6D, E). These results suggest that osteoblast metabolic reprogramming, especially the suppression of FAO, occurs after exposure to these EVs. EVs reduced mitochondrial length but significantly increased intracellular LD accumulation in osteoblasts (Fig. 6F). These findings suggest that EVs may inhibit FAO and lead to reduced LD catabolism. EVs reduced Cpt2 protein levels but had no significant effect on Cpt1 protein levels (Fig. 6G–I). EVs also inhibited the mRNA expression levels of the FAO rate-limiting enzymes Hadha, Acot13, and Echs1 to varying degrees (Fig. 6J–L). Furthermore,

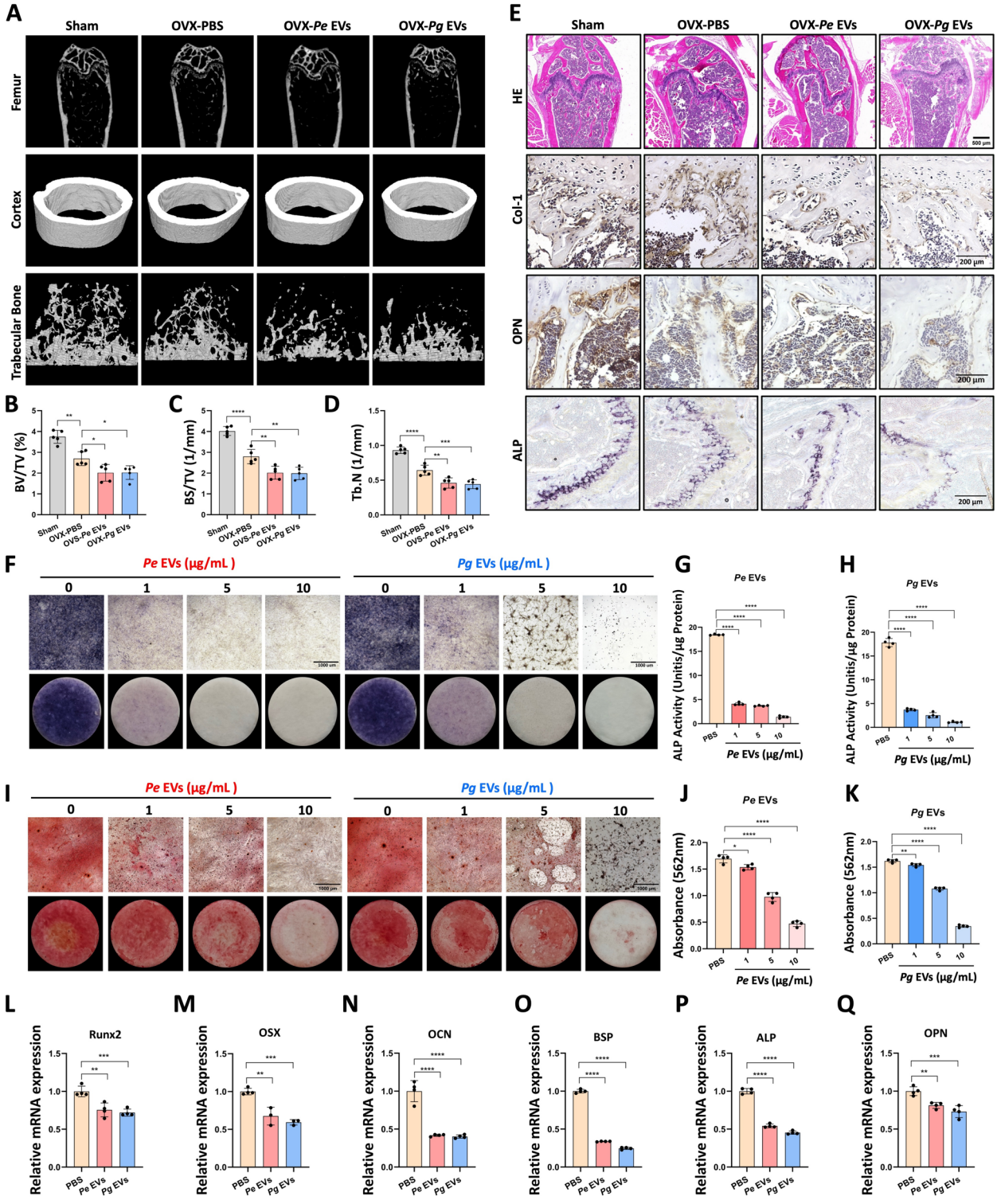

Fig. 2 *Pg* EVs and *Pe* EVs inhibited osteoblast differentiation and exacerbated osteoporosis. (**A**) From top to bottom: CT images of the mouse femur; 3D reconstruction of cortical bone; and 3D reconstruction of trabecular bone. (**B**) Bone volume fraction (BV/TV: bone volume/tissue volume) of femurs. (**C**) Bone surface fraction (BS/TV: bone surface area/tissue volume) of femurs. (**D**) Trabecular number of femurs. (**E**) Pathological staining of distal femurs: HE staining; Col-1 immunohistochemistry; OPN immunohistochemistry; and ALP staining (from top to bottom). (**F**–**H**) ALP staining (F, upper panel: microscopic view; lower panel: macroscopic view) and quantitative analysis of ALP activity (**G**, **H**) in MC3T3-E1 cells treated with different concentrations of EVs for 10 days. (**I**) Alizarin red staining (upper panel: microscopic view; lower panel: macroscopic view) of MC3T3-E1 cells treated with different concentrations of EVs for 21 days. (**J**, **K**) Semiquantitative analysis of Alizarin red staining in (I). (**L**–**Q**) mRNA expression levels of osteoblast differentiation marker genes in MC3T3-E1 cells treated with EVs for 3 days (**L**, **M**) or 7 days (**N**-**Q**). $^{*}P<0.05$, $^{**}P<0.01$, $^{***}P<0.001$, $^{****}P<0.0001$

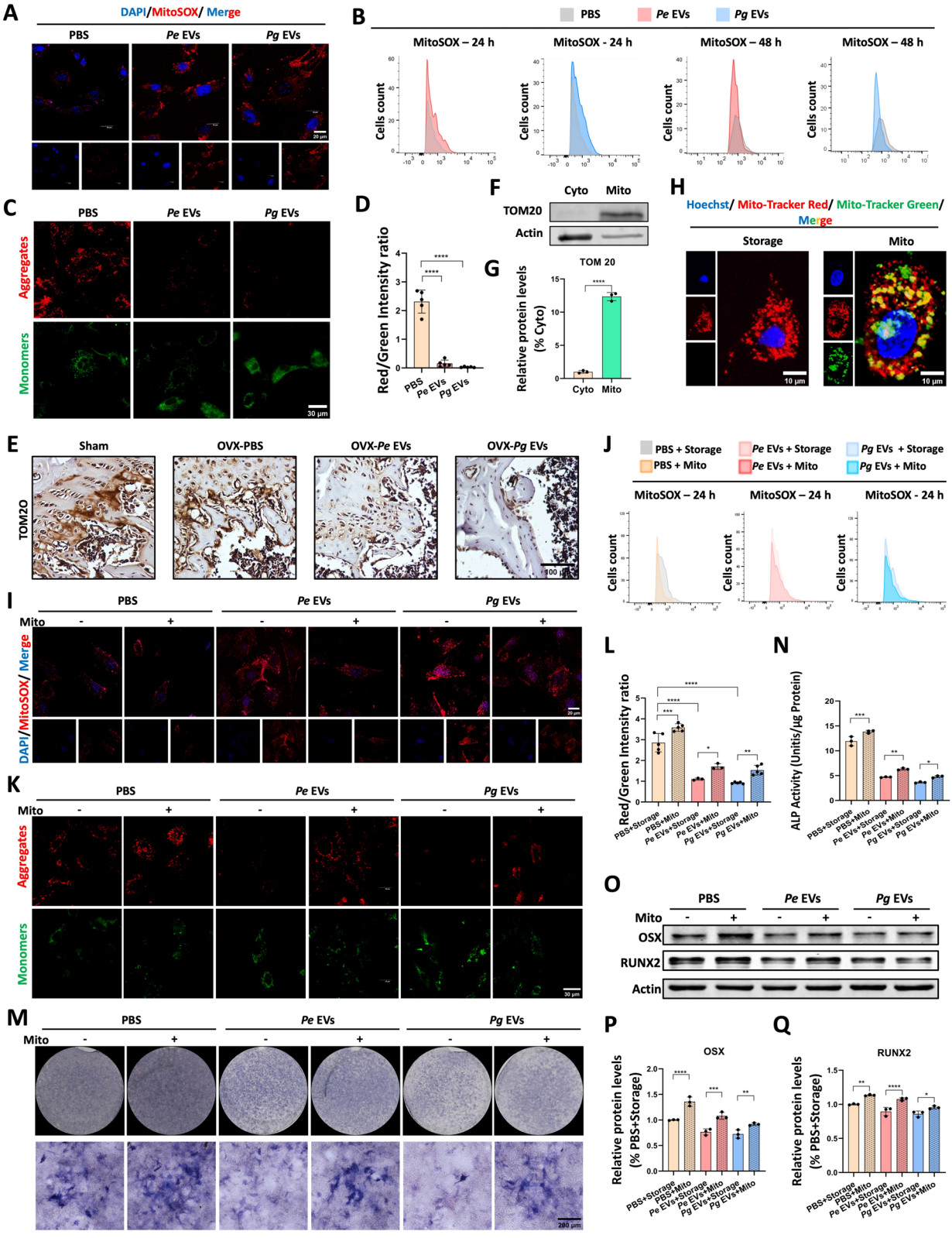

Fig. 3 (See legend on next page.)

(See figure on previous page.)

Fig. 3 *Pg* EVs and *Pe* EVs inhibited osteoblast differentiation by impairing mitochondrial activity. (**A**, **B**) Mitochondrial ROS were detected by using MitoSOX Red (red fluorescence), and nuclei were labeled with Hoechst (blue fluorescence). Confocal microscopy images (**A**) and flow cytometry analysis (**B**) showing the fluorescence intensity of ROS in MC3T3-E1 cells after treatment with EVs. (**C**) MMP was assessed via JC-1 staining in MC3T3-E1 cells after stimulation with EVs for 3 days; confocal microscopy images are shown. (**D**) The ratio of red to green fluorescence intensity after JC-1 staining was analyzed with Fiji software. (**E**) Immunohistochemical staining for TOM20 in trabecular bone. (**F**) Mitochondrial and cytoplasmic proteins were isolated from MC3T3-E1 cells after 5 days in differentiation culture, and WB analysis was performed to detect TOM20 expression. (**G**) Fiji software was used to analyze the relative protein expression of TOM20. (**H**) MitoTracker Green-labeled exogenous mitochondria (green fluorescence), MitoTracker Red-labeled recipient cell mitochondria (red fluorescence), and Hoechst-labled nuclei (blue fluorescence) are shown. Mitochondrial integration was observed via fluorescence microscopy. (**I**, **J**) Mitochondrial ROS was labeled with MitoSOX Red (red fluorescence) and nuclei were labeled with Hoechst (blue fluorescence). After the addition of exogenous mitochondria, confocal microscopy (**I**) and flow cytometry (**J**) were performed to detect the effect of EVs on mitochondrial ROS. (**K**) JC-1 staining was conducted after the addition of exogenous mitochondria. (**L**) The ratio of red to green fluorescence intensity after JC-1 staining. (**M**, **N**) After the addition of exogenous mitochondria, MC3T3-E1 cells were treated with EVs for 10 days, and ALP staining (**M**) and ALP activity (**N**) assays were performed. (**O**) Protein expression of OSX and RUNX2 was assessed via WB. (**P**, **Q**) Relative protein expression of OSX and RUNX2. $^{*}P < 0.05$, $^{**}P < 0.01$, $^{***}P < 0.001$, $^{****}P < 0.0001$

in OVX mice treated with EVs, the serum ATP and FFA levels were further decreased compared with those in the OVX group (Fig. 6M, N), and the expression level of Cpt2 in the bone was also further reduced (Fig. 6O). These results revealed that *Pg* EVs and *Pe* EVs reduced Cpt2 protein levels, inhibited FFA oxidation, and weakened the ATP production capacity of osteoblasts.

Pg EVs and Pe EVs inhibited osteoblast Cpt2 expression and FFA oxidation by disrupting mitochondrial dynamics

We nest investigate the relationship between mitochondrial dynamics and Cpt2 expression/FFA oxidation. Exogenous mitochondria partially reversed the increase in Drp1 expression and the reduced Mfn1 and Cpt2 expression induced by EVs (Fig. 7A-D). Compared with the control treatment (NC), Mfn1 and Opa1 co-overexpression led to increased Cpt2 expression in the EV groups (Fig. 7E, F). The co-overexpression of Mfn1 and Opa1 also increased the mitochondrial length, decreased the number of intracellular LDs (Fig. 7G), restored the mRNA expression levels of Hadha, Acot13, and Echs1 (Fig. 7H–J), recovered intracellular FFA levels (Fig. 7K), and increased ATP production (Fig. 7L). Similarly, knockdown of Drp1 and Fis1 in the presence of EVs reduced the suppression of Cpt2 expression (Fig. 7M, N), increased mitochondrial length, decreased LD numbers (Fig. 7O), restored the expression levels of FFA oxidation rate-limiting enzyme-encoding genes (Fig. 7P–R), restored intracellular FFA levels (Fig. 7S), and ultimately increased ATP production (Fig. 7T). These results suggest that *Pg* EVs and *Pe* EVs disrupt mitochondrial dynamics, thereby inhibiting Cpt2-mediated FFA oxidation. The addition of exogenous mitochondria, the upregulation of mitochondrial fusion or the downregulation of mitochondrial fission can increase both Cpt2 expression and FFA catabolism, thus decreasing LD formation and ultimately increasing osteoblast ATP production.

Pg EVs and Pe EVs inhibited osteoblast differentiation and exacerbated osteoporosis by suppressing Cpt2-regulated FFA oxidation

We nest verify whether EVs inhibited osteoblast differentiation by regulating Cpt2 and modulating FFA oxidation. Cpt2 overexpression in MC3T3-E1 cells partially increased the levels of FFAs (Fig. 8A), the mRNA levels of enzymes that regulate FFA oxidation (Fig. 8B–D) and the FAO activity (Fig. 8E, F), which were previously shown to be suppressed by EVs. ATP production was also partially restored (Fig. 8G). Cpt2, BSP, and RUNX2 expression levels were partially restored in osteoblasts treated with EVs after Cpt2 overexpression (Fig. 8H–K). A significant increase in ALP activity was observed (Fig. 8L, M). The overexpression of Cpt2 also alleviated the inhibitory effect of EVs on ALP activity in mouse primary calvarial osteoblasts (Fig. S13). However, Cpt2 overexpression did not reverse the inhibition of Mfn1 and Mfn2 or the promotion of Drp1 induced by EVs (Fig. S14A–D), which suggested that Cpt2 is a downstream regulatory protein of mitochondrial dynamics. These results indicated that Cpt2 overexpression alleviated the inhibitory effects of *Pg*-EVs and *Pe*-EVs on FFA oxidation and differentiation in osteoblasts.

To further determine the effects of Cpt2 on FAO and osteoblast differentiation in vivo, we injected AAV-packaged, RUNX2-targeted Cpt2 overexpression plasmids into the joint cavities of osteoporotic mice (Fig. 9A). Green fluorescence (EGFP) was observed in the femur of the mice that were injected with the AAV-NC or AAV-Cpt2 virus but not in those of the control mice without virus injection (Fig. S15). Analysis of mouse femur proteins confirmed successful Cpt2 overexpression (Fig. 9B, C). Serum analyses revealed that Cpt2 overexpression reversed the inhibitory effects of *Pg*-EVs and *Pe*-EVs on ATP and FFA levels in osteoporotic mice (Fig. 9D, E). Cpt2 overexpression partially reversed the decreases in bone trabecular number and density induced by EVs in osteoporotic mice (Fig. 9F–I). Cpt2 overexpression also restored the expression levels of the FFA oxidation-regulating enzyme Hadha and the osteogenic differentiation

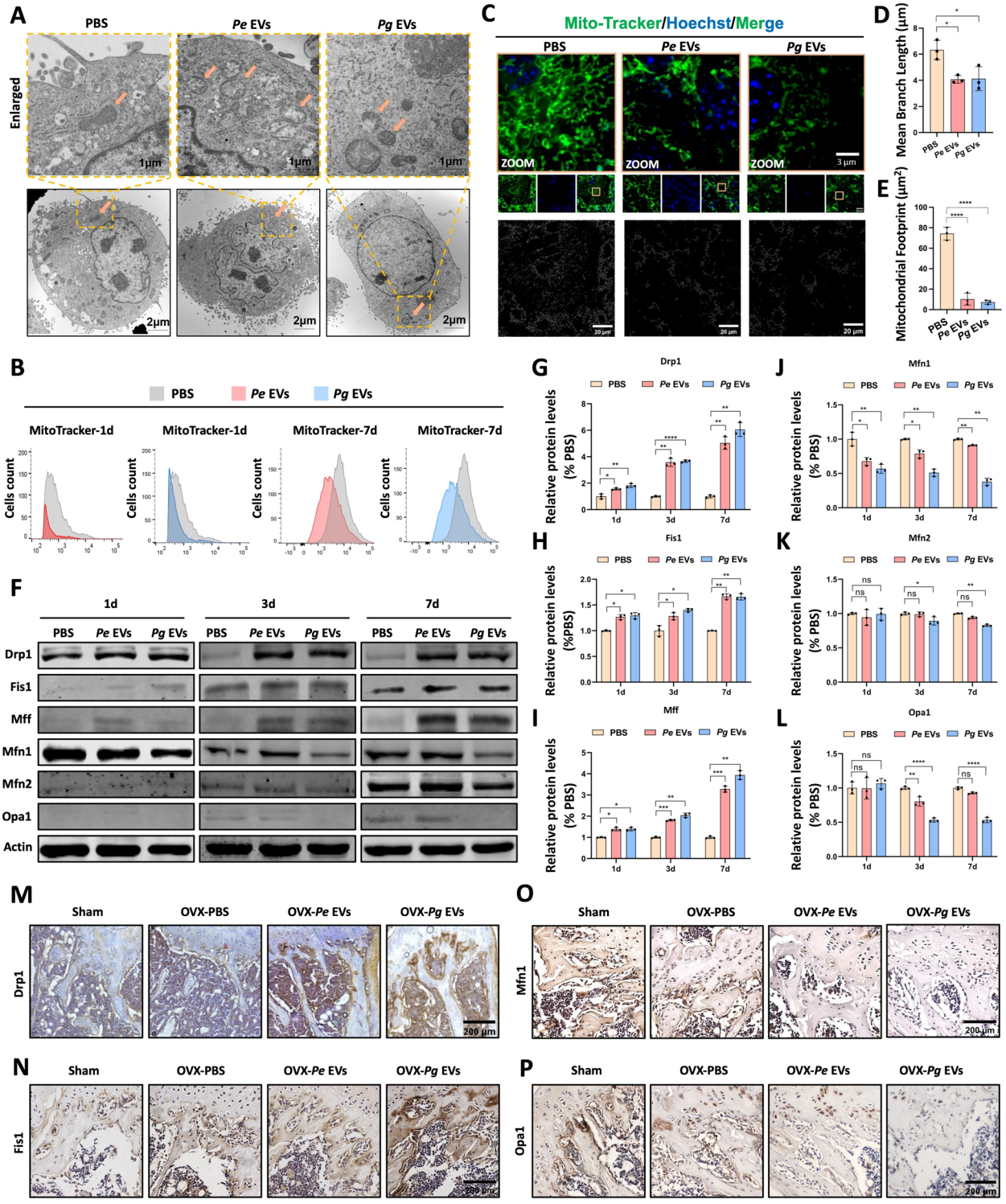

Fig. 4 *Pg* EVs and *Pe* EVs promoted mitochondrial fission and inhibited mitochondrial fusion in osteoblasts. (**A**) TEM was used to observe the mitochondrial morphology of MC3T3-E1 cells after treatment with EVs. (**B**) MitoTracker Green was used to label mitochondria, and flow cytometry was used to detect the mitochondrial fluorescence intensity of MC3T3-E1 cells after EV stimulation. (**C**) MitoTracker Green was used to label the mitochondria, and the nuclei were labeled with Hoechst (blue fluorescence). The upper row shows laser confocal images of the mitochondria, and the lower row shows the mitochondrial skeleton after processing with Fiji software. (**D**, **E**) Quantification of the mitochondrial network length and footprint. (**F**) WB analysis of Drp1, Fis1, Mff, Mfn1, Mfn2, and Opa1 protein expression in MC3T3-E1 cells after 1, 3, and 7 days of EV treatment. (**G–L**) Quantitative analysis of the WB data with Fiji software. (**M–P**) Immunohistochemical staining of Drp1, Fis1, Mfn1, and Opa1 in mouse femur sections. ns $P > 0.05$, $^{*}P < 0.05$, $^{**}P < 0.01$, $^{***}P < 0.001$, $^{****}P < 0.0001$

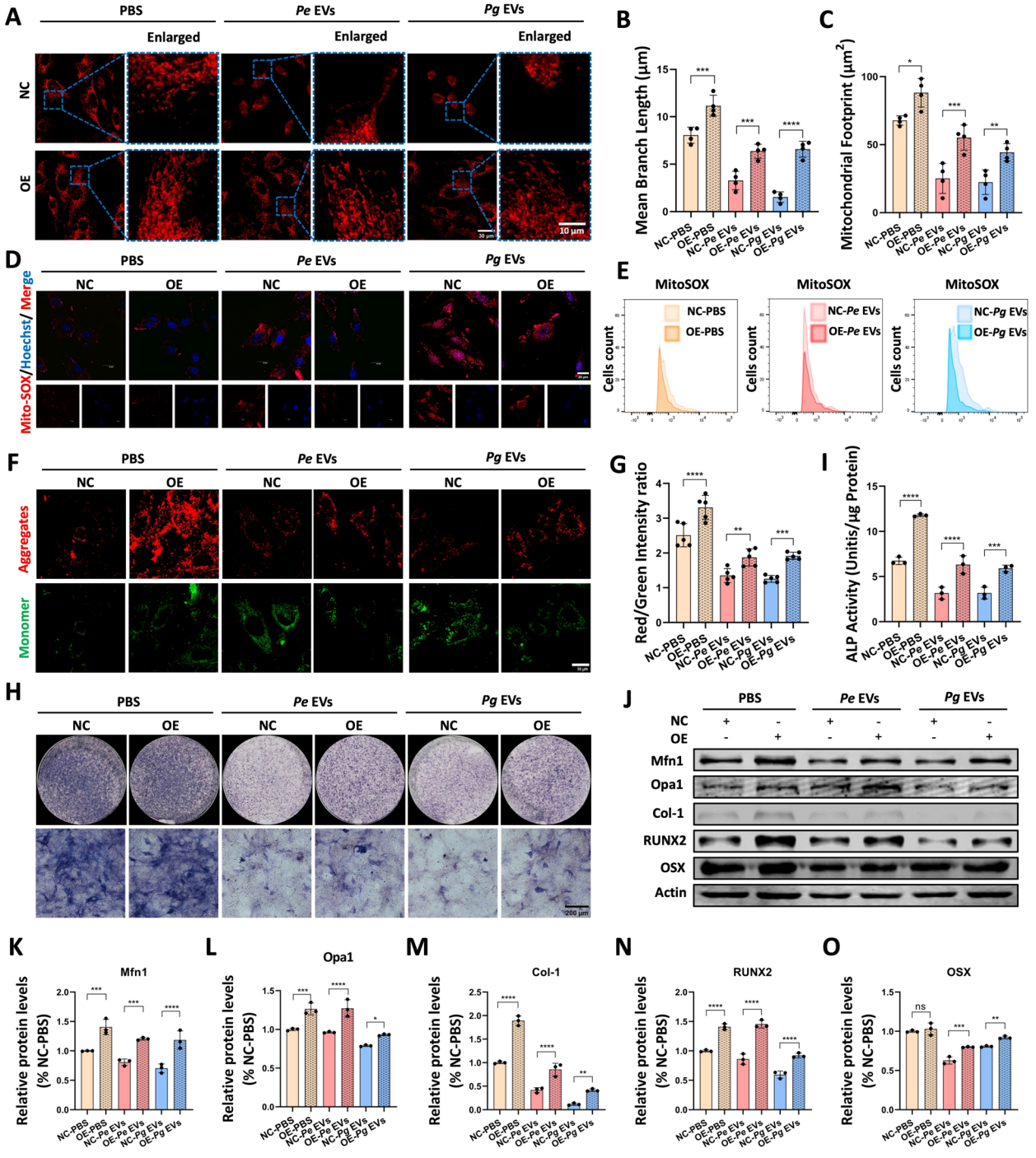

Fig. 5 The overexpression of Mfn1 and Opa1 partially rescued *Pg*-EV- and *Pe*-EV-induced disruption of mitochondrial activity and osteoblast differentiation. After co-overexpression of Opa1 and Mfn1, MC3T3-E1 cells were treated with EVs for the indicated times. (**A**) Mitochondria were labeled with Mito-Tracker Red and observed by laser confocal microscopy. (**B**) Mitochondrial skeleton length analysis. (**C**) Mitochondrial footprint analysis. (**D**) After 1 day of treatment, mitochondrial ROS were labeled with MitoSOX Red and observed by fluorescence confocal microscopy; nuclei were labeled with Hoechst. (**E**) After 1 day of treatment, the labeling of mitochondrial ROS with MitoSOX Red was analyzed by flow cytometry. (**F**) After 3 days of treatment, JC-1 staining was performed to determine the MMP. (**G**) Red–green fluorescence intensity ratio after JC-1 staining. (**H–J**) After 10 days of treatment, ALP staining (**H**), ALP activity assays (**I**), and WB analysis of the protein expression of Mfn1, Opa1, Col-1, RUNX2 and OSX (**J**) were performed. (**K–O**) Fiji software was used to analyze the relative expression of the Mfn1, Opa1, Col-1, RUNX2, and OSX proteins. "OE" in all the graphs represents co-overexpression of Mfn1 and Opa1, and "NC" represents the blank control. ns $P > 0.05$, $^{*}P < 0.05$, $^{**}P < 0.01$, $^{***}P < 0.001$, $^{****}P < 0.0001$

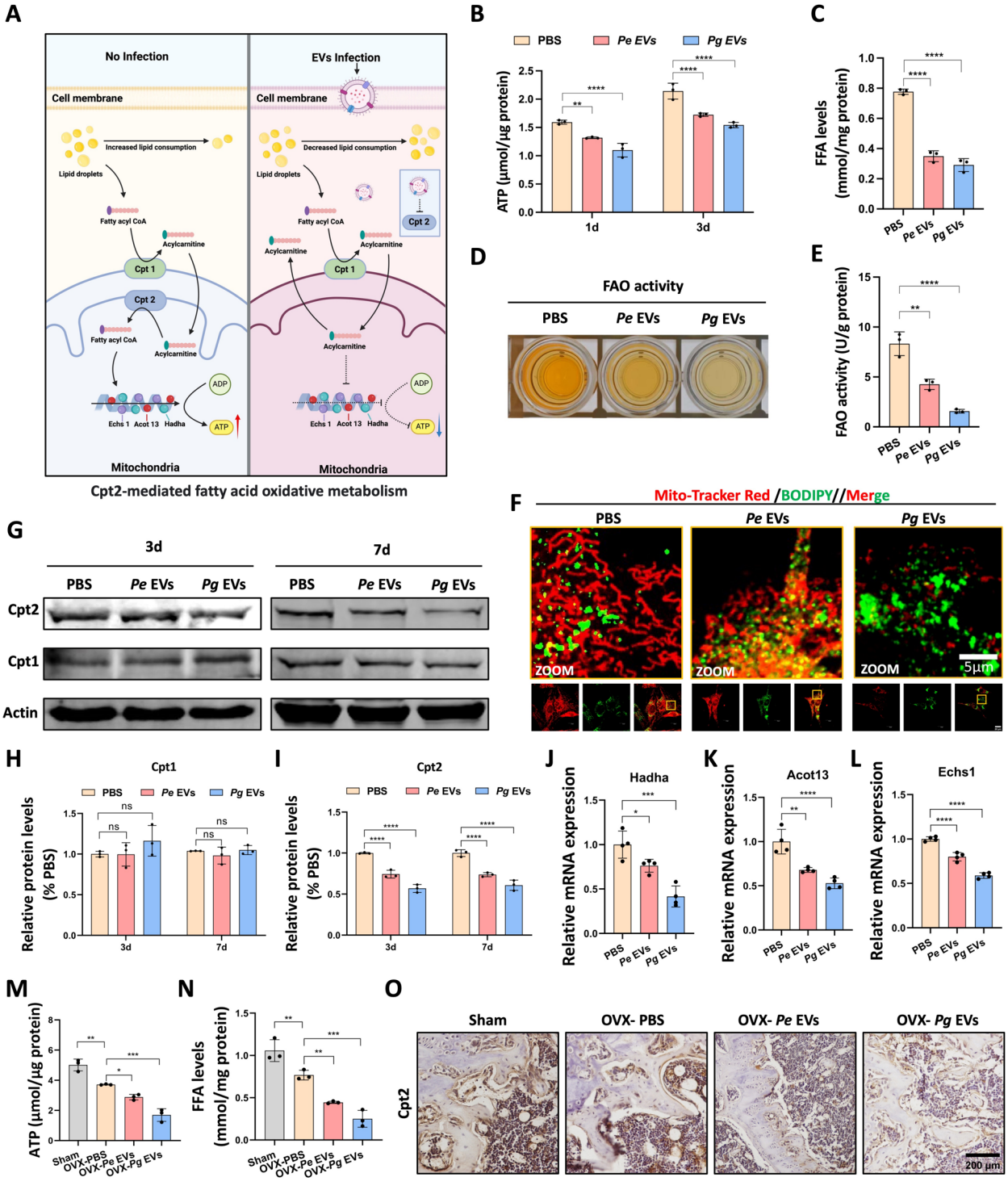

Fig. 6 *Pg* EVs and *Pe* EVs inhibited Cpt2 expression, FFA oxidation, and ATP production in osteoblasts. (**A**) Schematic diagram of the mechanism by which mitochondrial FAO is regulated by Cpt2 under physiological conditions or after EV treatment. (**B**) Intracellular ATP levels in MC3T3-E1 cells after EV treatment for 1 and 3 days. (**C**) Intracellular FFA levels in MC3T3-E1 cells after EV treatment for 7 days. (**D**) Photographs of the plates used for the FAO experiment after EV treatment for 3 days. (**E**) FAO activity analysis after EV treatment for 3 days. (**F**) Effects of EVs on mitochondrial morphology and LD numbers; mitochondria were labeled with MitoTracker Red (red fluorescence), and LDs were labeled with BODIPY (green fluorescence). (**G**) WB analysis of Cpt1 and Cpt2 protein level in MC3T3-E1 cells after EV treatment for 3 and 7 days. (**H**, **I**) Quantitative analysis of Cpt1 and Cpt2 protein level. (**J**–**L**) mRNA expression levels of the FAO-regulating enzymes Hadha, Acot13, and Echs1 in MC3T3-E1 cells after EV treatment for 7 days. (**M**–**O**) Serum ATP levels (**M**), serum FFA levels (**N**), and immunohistochemical staining to evaluate Cpt2 protein expression in femur sections (**O**) from osteoporotic mice after EV treatment. ns $P > 0.05$, $^{*}P < 0.05$, $^{**}P < 0.01$, $^{***}P < 0.001$, $^{****}P < 0.0001$

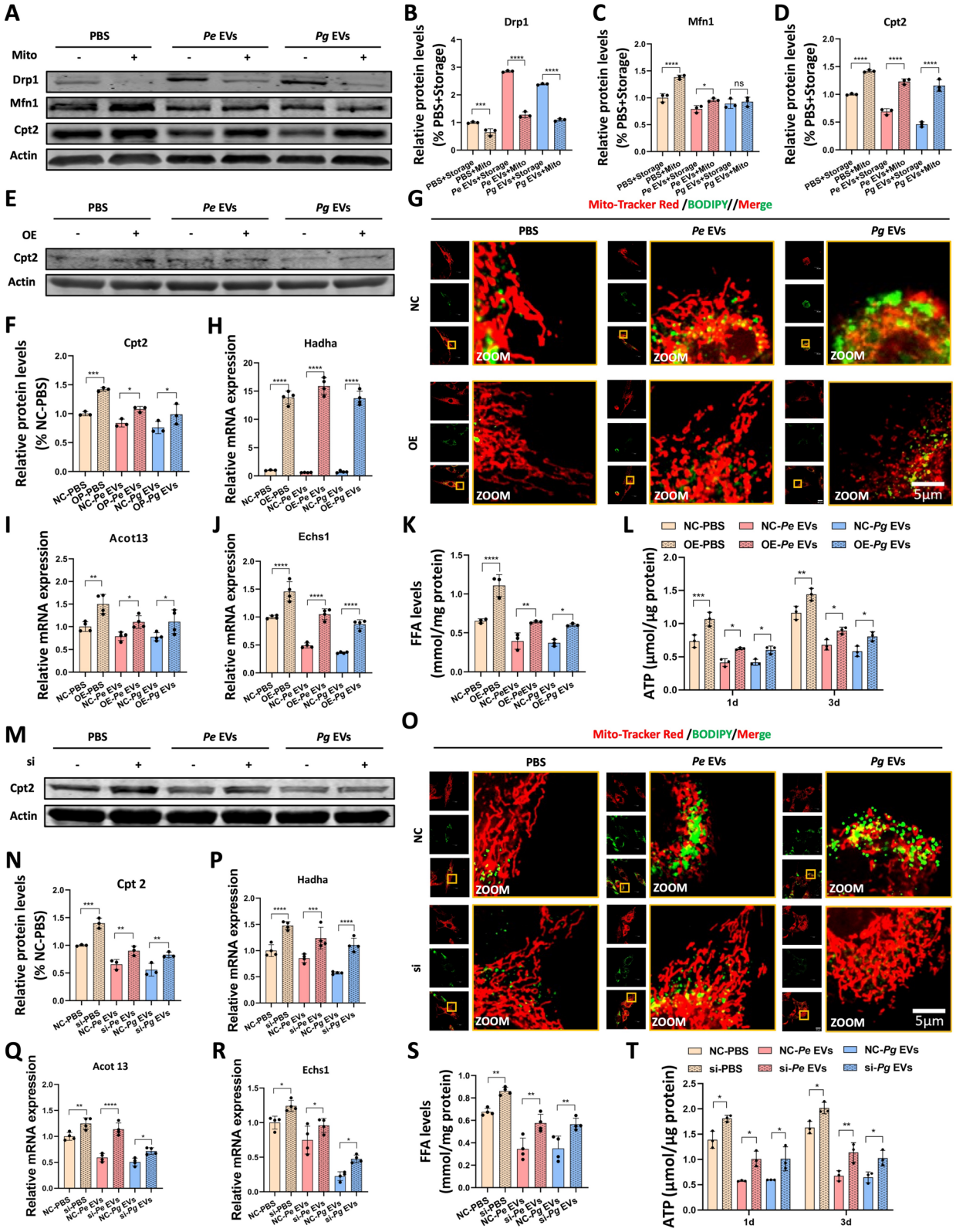

Fig. 7 (See legend on next page.)

(See figure on previous page.)

Fig. 7 Modulation of mitochondrial dynamics partially reversed the inhibition of Cpt2 expression and FFA oxidation observed in EV-treated osteoblasts. (**A–D**) Addition of exogenous mitochondria to EV-treated MC3T3-E1 cells. (**A**) Protein expression of Drp1, Mfn1, and Cpt2. (**B–D**) Quantitative analysis of Drp1, Mfn1, and Cpt2 protein expression. (**E–K**) After co-overexpressing Mfn1 and Opa1, MC3T3-E1 cells were treated with EVs for 7 days. (**E**) WB analysis of Cpt2 protein expression. (**F**) Quantitative analysis of Cpt2 protein expression. (**G**) Mitochondrial morphology and LD numbers were observed by confocal microscopy; mitochondria were labeled with MitoTracker Red, and LDs were labeled with BODIPY (green fluorescence). (**H–J**) mRNA expression of Hadha, Acot13, and Echs1. (**K**) Intracellular FFA levels. (**L**) Intracellular ATP levels in EV-treated MC3T3-E1 cells after co-overexpression of Mfn1 and Opa1. (**M–S**) After knockdown of Drp1 and Fis1, MC3T3-E1 cells were treated with EVs for 7 days. (**M**) WB analysis of Cpt2 protein expression. (**N**) Quantitative analysis of Cpt2 protein expression. (**O**) Mitochondrial morphology and the number of LDs were observed by confocal microscopy. (**P–R**) mRNA expression of Hadha, Acot13, and Echs1. (**S**) Intracellular FFA levels. (**T**) Intracellular ATP levels in EV-treated MC3T3-E1 cells after knockdown of Drp1 and Fis1. "OE" indicates co-overexpression of Mfn1 and Opa1, and "si" indicates simultaneous knockdown of Drp1 and Fis1. ns $P > 0.05$, $^{*}P < 0.05$, $^{**}P < 0.01$, $^{***}P < 0.001$, $^{****}P < 0.0001$

marker protein OPN in EV-treated osteoporotic mice (Fig. 9J). Collectively, our findings demonstrated that *Pg* EVs and *Pe* EVs hindered osteoblast differentiation and exacerbated osteoporosis by inhibiting Cpt2-mediated FFA oxidation. The overexpression of Cpt2 effectively mitigated the ability of *Pg* EVs and *Pe* EVs to inhibit osteoblast differentiation and promote osteoporosis.

Discussion

PD and osteoporosis are age-related bone diseases. Although previous studies have focused on how osteoporosis exacerbates periodontal bone loss in PD patients, the impact of PD on osteoporosis remains poorly understood. This study innovatively explores the pathogenic mechanism through which circulating EVs from *Pg*, a key PD pathogen, aggravate osteoporosis. Our findings demonstrate that *Pg* EVs can be transported into the marrow cavity of the long bones via the circulatory system and internalized by osteoblasts. EVs subsequently disrupt mitochondrial dynamics, which leads to mitochondrial fragmentation and impaired mitochondrial function. In particular, EVs reduce Cpt2 protein levels and disrupt FAO. All these factors result in impaired ATP production, ultimately inhibiting osteoblast differentiation and exacerbating osteoporosis.

EVs released by bacteria are small in size and large in quantity and can be easily internalized into cells [31]. The high lipid content of the EV membrane allows entry into host cells via lipid rafts, increasing uptake efficiency [10, 32, 33], as demonstrated by our experimental results. The presence of protective enzymes makes EVs reduces the impact of environmental stress, resistant to degradation and neutralization by host antibodies, which can effectively prolong the stability and activity of the encapsulated virulence factors [34, 35]. During EV biogenesis, bacterial components are selectively enriched, resulting in a stronger pathogenic effect per unit for EVs [36]. These characteristics enable EVs to act as "long-range weapons" for bacteria. Numerous studies have demonstrated that oral bacteria-derived EVs can be transported to the brain [12, 13, 37], bones [14], liver [9], or adipose tissue [38] via blood-mediated pathways. For EVs originating from periodontal pathogens, the probability of entering the bloodstream significantly increases following surgical treatment or scaling, as well as when bacterial activity disrupts endothelial cell junctions [39]. Therefore, we referred to previous studies that utilized intraperitoneal injection to simulate the blood transport of oral bacterial EVs to investigate their relationship with systemic diseases [9, 14, 38, 40]. Compared with periodontal injection, intraperitoneal injection of EVs overcomes the leakage associated with local periodontal administration and the nonspecific infection concerns related to *Pg* EVs or *Pe* EVs [37]. Additionally, intraperitoneal injection of EVs allows for their absorption into the systemic circulation via the peritoneum, a process that is generally slower than intravenous administration, thereby providing a more sustained concentration of EVs for infection. Intraperitoneal injection can accommodate larger volumes of low-concentration EV solutions, thereby avoiding the acute vascular inflammatory responses or thrombosis risks associated with small-volume, high-concentration intravenous injections [41]. Additionally, because in vivo experiments often require multiple consecutive injections of EVs, intraperitoneal administration enhances the success rate of injections and ensures consistency in the quantity of delivered EVs. Intraperitoneal administration mitigates issues such as EV leakage, uneven distribution, and the inability to immediately reinject, which may arise from failed intravenous injections [42]. For determination of the EV concentration, we referred to the relevant literature. These studies employed 3 μg/μL *Pg* EVs and 1 μg/μL *Fusobacterium nucleatum* EVs to infect cells [43, 44]. We found that at a minimum concentration of approximately 1 μg/μL, the inhibitory effects of EVs on osteoblast differentiation were relatively stable. In the in vivo experiments, the total amount of EVs injected per mouse was 20 μg, with each mouse weighing approximately 20 g, resulting in an injection dose of 1 μg/g body weight. With respect to the injection concentration of EVs, we opted for 0.2 μg/μL and avoided concentrations above 1 μg/μL primarily to minimize the occurrence of peritoneal inflammation and other toxic reactions. Additionally, based on a previous study investigating the transport of oral bacterial EVs to the bone marrow cavity in mice [14], we administered injections every three days.

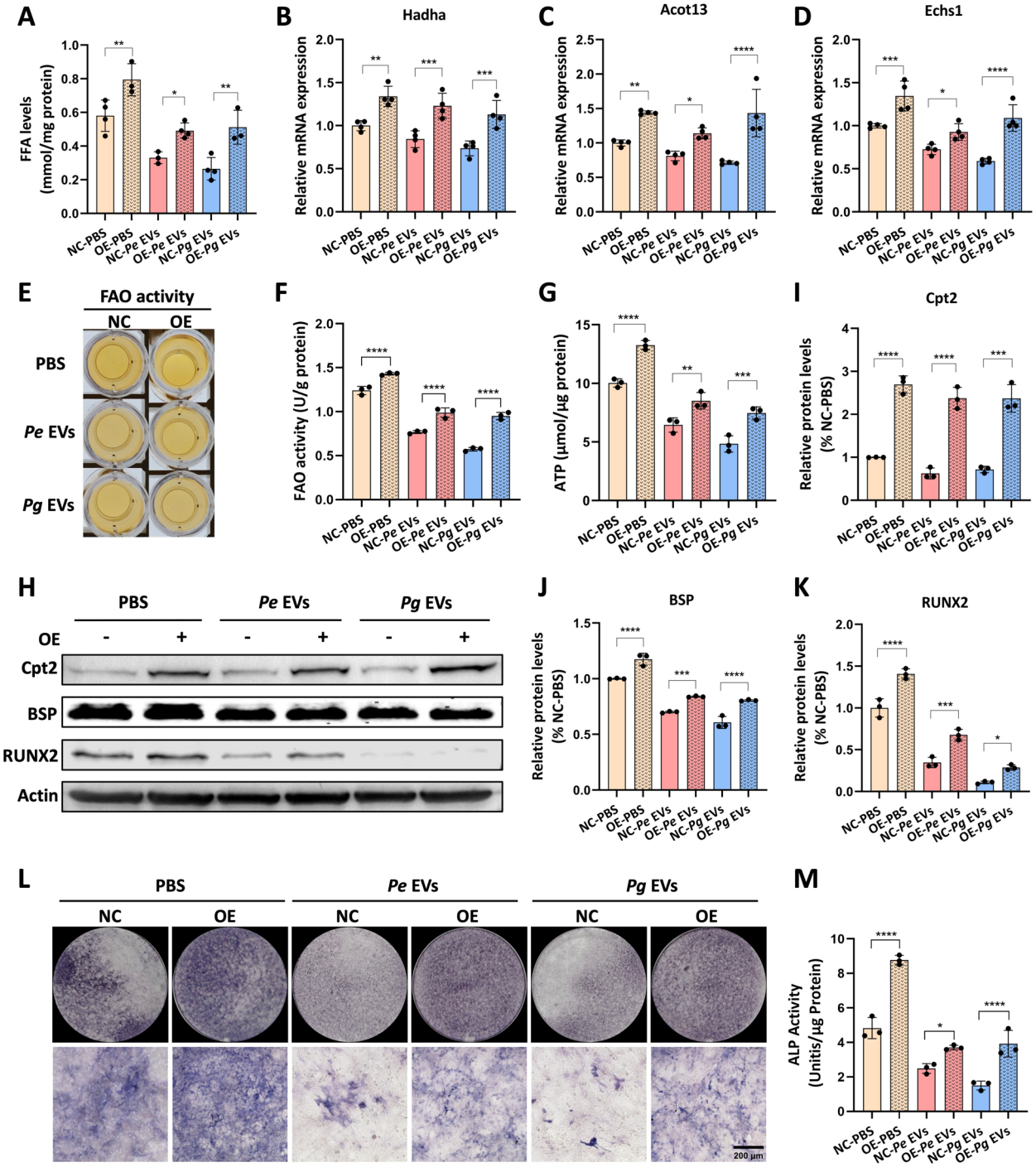

Fig. 8 Cpt2 overexpression partially reversed the inhibitory effects of *Pg*-EVs and *Pe*-EVs on FFA oxidation and osteogenic differentiation in osteoblasts. (**A**–**M**) After Cpt2 overexpression, MC3T3-E1 cells were treated with EVs for the indicated times. (**A**) Intracellular FFA levels after 7 days. (**B**–**D**) mRNA expression levels of Hadha, Acot13, and Echs1 after 7 days. (**E**) Photographs of the plates for the FAO experiment after 3 days. (**F**) FAO activity analysis after 3 days. (**G**) Intracellular ATP levels after 3 days. (**H**) Protein expression of Cpt2, BSP, and RUNX2 after 7 days. (**I**–**K**) Quantitative analysis of Cpt2, BSP, and RUNX2 protein expression. (**L**) ALP staining after 10 days. (**M**) ALP activity after 10 days. $^{*}P<0.05$, $^{**}P<0.01$, $^{***}P<0.001$, $^{****}P<0.0001$

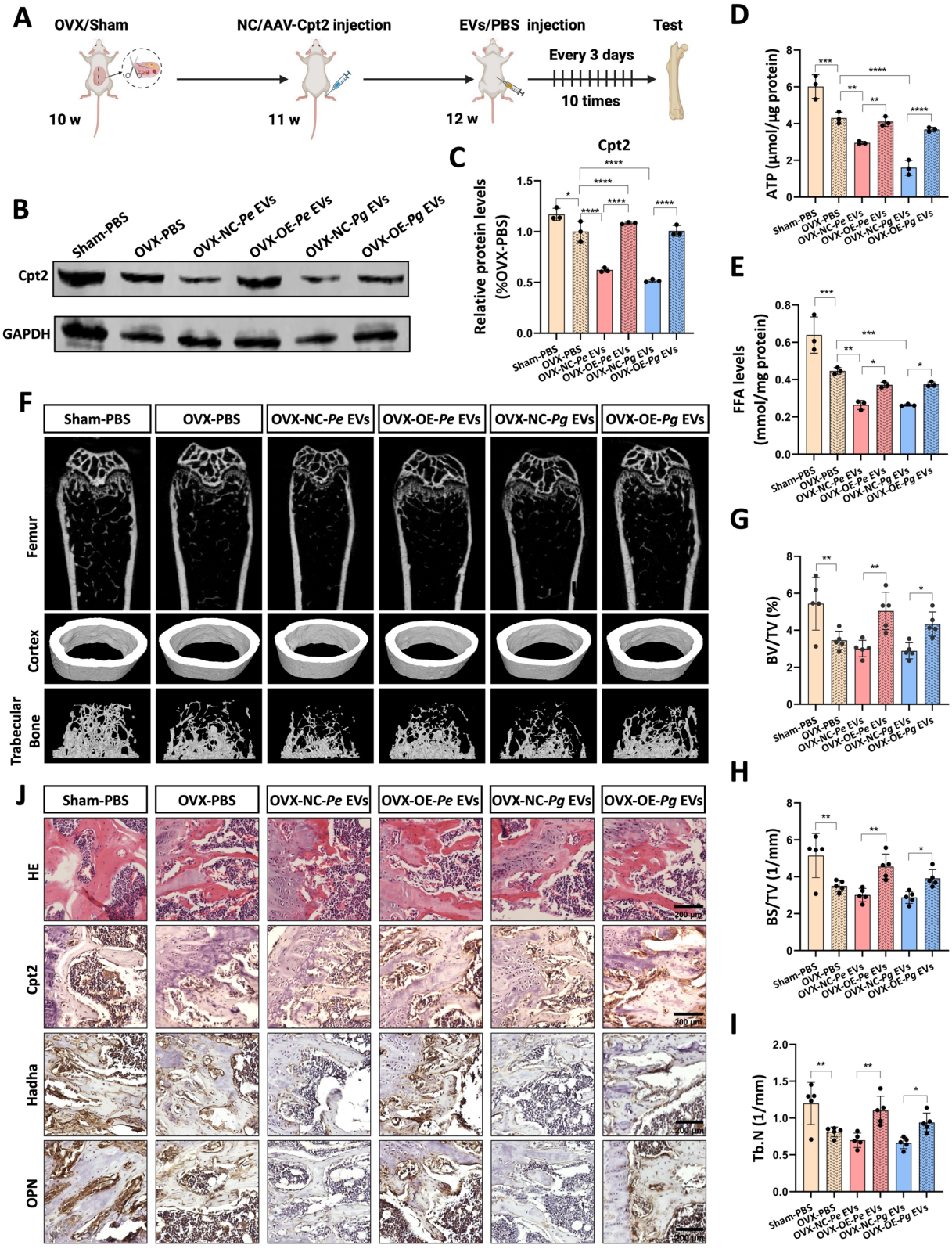

Fig. 9 (See legend on next page.)

(See figure on previous page.)

Fig. 9 Targeted overexpression of Cpt2 in osteoblasts alleviates osteoporosis exacerbated by *Pg* EVs and *Pe* EVs. (**A**) Schematic diagram of a mouse injected with EVs with or without AAV-Cpt2. (**B**) WB analysis of Cpt2 protein expression in bone from osteoporotic mice after AAV-Cpt2 transfection. (**C**) Quantitative analysis of Cpt2 protein expression. (**D**) Serum ATP levels in the mice. (**E**) Serum FFA levels in the mice. (**F**) 3D reconstructions of mouse femur CT images; from top to bottom, cortical bone and trabecular bone are shown. (**G**) Bone volume fraction. (**H**) Bone surface area fraction. (**I**) Bone trabecular number. (**J**) Histological analysis of mouse femur sections: HE staining and immunohistochemistry for Cpt2, Hadha, and OPN. "OE" represents Cpt2 overexpression, and "NC" represents the empty vector control. $^{*}P < 0.05$, $^{**}P < 0.01$, $^{***}P < 0.001$, $^{****}P < 0.0001$

In present study, similar to the pathogenic characteristics of EVs from other oral bacteria [7, 13, 14], both *Pg* EVs and *Pe* EVs can be transported to the bone marrow cavity within 3 h and rapidly internalized by osteoblasts via clathrin-and lipid raft-mediated endocytic pathways. In summary, our study proposes a pathogenic pathway in which *Pg* EVs are transported to distant osteoblasts via bodily fluids, directly enter bone, and ultimately exacerbate osteoporosis.

Pg can influence mitochondrial activity in various periodontal cells [45]. A healthy mitochondrial morphology ensures stable mitochondrial activity, which is crucial for cellular resistance to inflammation and the oxidative burst and for promoting bone formation [46]. Mitochondrial fusion, which is primarily mediated by the outer membrane fusion of Mfn1 and Mfn2 and the inner membrane fusion of Opa1, results in the merging of two adjacent mitochondria into a single elongated mitochondria [47]. This facilitates the transfer and sharing of energy and material [48]. Mitochondrial fission, which is regulated by Drp1, Fis1, and Mff, can generate two mitochondria through division [49, 50]. Moderate mitochondrial fission favors the removal of damaged mitochondria, while excessive mitochondrial fission leads to mitochondrial fragmentation and impaired activity [51]. Studies have shown that *Pg* promotes mitochondrial fission but does not affect on fusion in endothelial cells [52]. In our study, *Pg* EVs promoted fission while inhibited fusion, resulted in excessive mitochondrial fragmentation and severe impairment of osteoblast activity. The promotion of Pink1 and Parkin expression by EVs suggests that excessive mitochondrial fission leads to a compensatory increase in mitophagy [53]. Conversely, supplementation with exogenous mitochondria, upregulation of mitochondrial fusion or downregulation of mitochondrial fission could restore the disrupted mitochondrial homeostasis induced by *Pg* EVs and subsequently promote osteoblast differentiation. These results are consistent with previous findings [46]. In conclusion, our study not only elucidate the mechanism by which *Pg* EVs inhibit osteogenic differentiation but also expand the theoretical understanding of the mechanism by which *Pg* regulates mitochondrial dynamics in host cells.

Mitochondria are central to various metabolic activities, including OXPHOS, FAO, and amino acid degradation, and are the primary site of ATP synthesis [54]. Previous research has shown that bacterial infection leads to mitochondrial fragmentation, and induces metabolic reprogramming in cells to enable adaptation to the altered environment [55]. The role of OXPHOS in osteoblast differentiation is well established and understood [56, 57]; however, studies on FAO in osteoblasts are relatively limited, particularly with respect to whether *Pg* EV-induced mitochondrial damage inhibits the FAO process in osteoblasts. Osteoblasts utilize LDs and generate FFAs that undergo FAO for energy production. FAO activates FFAs into acyl-CoA, which undergoes β-oxidation in mitochondria to produce ATP. FAO upregulation reduces intracellular LD accumulation, while inhibiting FFA catabolism impairs osteoblast differentiation and increases LD abundance [58, 59]. Our findings demonstrated that *Pg* EVs inhibited osteoblast mitochondrial oxidative respiration and increased the expression of key glycolytic enzyme-encoding genes. Importantly, *Pg* EVs suppressed intracellular FFA levels and FAO activity in osteoblasts, decreased the expression of key fatty acid β-oxidation rate-limiting enzymes, and reduced ATP production. This reduced FFA catabolism led to lower utilization of LDs and the buildup of LDs around the mitochondria. Therefore, our study innovatively shows that *Pg* EV-induced mitochondrial damage can inhibit osteoblast differentiation by impeding FAO. Previous studies have indicated that supplementation with fatty acids can increase osteoblast energy production and improve bone loss in osteoporosis [56, 60–62]. Therefore, modulating FAO can alleviate the promoting effect of *Pg* EVs on osteoporosis.

We further explored how *Pg* EV-mediated modulation of mitochondrial dynamics affects the FAO process in osteoblasts. FFA is activated in the cytoplasm to form acyl-CoA. Cpt1 and Cpt2, both nucleus-encoded proteins, are synthesized in the cytoplasm and then transported to the mitochondria [63]. Cpt1, which is located on the outer mitochondrial membrane, converts cytoplasmic acyl-CoA to acylcarnitine for transport into the mitochondria [64]. Cpt2, which is located on the inner mitochondrial membrane, converts acylcarnitine back to acyl-CoA and enables FAO. Studies have shown that Mfn2 overexpression in hepatocytes promotes mitochondrial fusion and inhibits Cpt1-mediated FAO [65]. Maintaining the physiological morphology of mitochondria is crucial for maintaining the energy metabolic balance. Our study indicated that promoting mitochondrial fission in osteoblasts inhibited Cpt2-mediated FAO.

Among the investigated regulators of mitochondrial dynamics, *Pg* EVs most significantly suppressed the inner mitochondrial membrane fusion protein Opa1. WB analysis revealed almost no detectable Opa1 protein expression. This may lead to severe impairment of inner mitochondrial membrane fusion, which can reduce crista abundance and disrupt the binding site for Cpt2 on the inner membrane. Cpt2, which detaches from the inner mitochondrial membrane, becomes unstable and susceptible to ubiquitination by the E3 ubiquitin ligase HRD1 and is subsequently degraded [66, 67]. Consequently, acylcarnitine cannot be converted to acyl-CoA by Cpt2, which can lead to substrate deficiency, FAO suppression, and ATP deficiency. Conversely, Cpt2 overexpression, both in vitro and in vivo, increased FAO, restored ATP levels, and attenuated the inhibitory effects of *Pg* EVs on osteoblast differentiation and osteoporosis in mice. These findings provide a new understanding of the changes in osteoblast energy metabolism that occur during infection and identify a reliable regulatory target for osteoporosis treatment.

Both *Pg* and *Pe* belong to the genus *Porphyromonas* and are frequently codetected in periodontal [68, 69] or periapical diseases [70, 71]. However, in previous studies on the etiology of PD, the focus has predominantly been on *Pg*, whereas the role of *Pe* has often been overlooked. Both *Pe* and *Pg* can produce acetate, malate dehydrogenase, and glutamate dehydrogenase. The key differences between them are as follows: *Pe* exhibits low proteolytic activity and can hydrolyze angiotensin and native proteins [72], whereas *Pg* contains the unique virulence factor gingipain and is the only prokaryote capable of producing peptidylarginine deiminase [73, 74]. Therefore, comparative studies of *Pg* and *Pe* not only help elucidate the common pathogenic mechanisms within the *Porphyromonas* genus but also reveal differences in pathogenic intensity among different subtypes of the same genus, aiding in the exploration of potential distinct virulence factors contributing to the pathogenicity of *Pg* and *Pe*. Furthermore, this study highlights the role of *Pe* in systemic disease associations, contributing to a re-evaluation the etiological contribution of *Pe* to PD. In this study, *Pg* EVs have stronger effects on mitochondrial dynamics, Cpt2 expression, and osteoblast inhibition than do *Pe*-EVs. Based on the results of the mass spectrometry analysis of EVs, it can be reasonably hypothesized that the unique virulence factors of *Pg* EVs, such as RgpA and RgpB, may contribute to the stronger inhibitory effect of *Pg* EVs on osteoblast differentiation compared with that of *Pe* EVs. However, *Pe* EVs at equivalent doses exhibited effects similar to those of *Pg* EVs. These findings suggest that the synergistic effects of common virulence factors among the *Porphyromonas* species, including but not limited to lipopolysaccharides, nucleic acids, phospholipids, and mass-unidentified coexpressed proteins, rather than individual virulence factors, may be the key to pathogenicity.

This study has several limitations. In the future, we should further identify the specific virulence factors that inhibit osteoblast differentiation in *Pg* EVs and *Pe* EVs and generate differentiated EVs through gene knockout technology. Furthermore, we should further investigate the dose–response relationship of EVs in vivo and compare the differences between local and systemic administration of EVs to more comprehensively demonstrate the physiological relevance of EVs to osteoporosis. In addition, the number of replicate samples in in vitro studies should be increased to ensure greater statistical power.

Conclusions

Pg and *Pe* secrete extracellular nanoscale vesicles. These EVs reach the bone marrow cavity via systemic circulation, where they act on osteoblasts, inhibiting osteoblast differentiation and promoting the development of osteoporosis. Mechanistically, after *Pg* EVs and *Pe* EVs are internalized by osteoblasts via clathrin- and lipid raft-mediated endocytic pathways, they promote mitochondrial fission (indicated by increased levels of DRP1, MFF, and FIS1) and inhibit mitochondrial fusion (indicated by decreased levels of MFN1, MFN2, and OPA1). This disrupts mitochondrial dynamics, leading to abnormal mitochondrial morphology, including mitochondrial fragmentation and damage. This damage manifests as a reduced MMP and increased ROS, causing mitochondrial dysfunction. Furthermore, the protein level of Cpt2 is downregulated, preventing acyl-CoA from being catalyzed into the mitochondria, impairing the fatty acid oxidation pathway, and hindering ATP production, ultimately inhibiting osteoblast differentiation. In summary, we innovatively propose a biological mechanism through which *Pg* EVs regulate osteoblast mitochondrial dynamics and FAO and aggravate osteoporosis. This study contributes to the understanding of the etiological mechanisms through which *Pg* contributes to the progression of osteoporosis and highlights the pivotal role of EVs in the association between periodontal disease and systemic diseases.

Abbreviations

PD	Periodontitis
Pg	*Porphyromonas gingivalis*
EVs	Extracellular vesicles
FAO	Fatty acid oxidation
Cpt1	Carnitine palmitoyl transferase 1
Cpt2	Carnitine palmitoyl transferase 2
Pe	*Porphyromonas endodontalis*
SEM	Scanning electron microscopy
TEM	Transmission electron microscopy
OmpA	Outer membrane protein A
RgpA	Gingipain R1
RgpB	Gingipain R2

MβCD	Methyl-β-cyclodextrin
FFA	Free fatty acid
BV	Bone volume
TV	Tissue volume
Tb.N	Trabecular number
Col-1	Collagen type I
OPN	Osteopontin
MMP	Mitochondrial membrane potential
Pink1	PTEN induced putative kinase 1
Parkin	Parkin RBR E3 ubiquitin protein ligase
WB	Western blotting
HE	Hematoxylin–eosin
Nd3	NADH Dehydrogenase Subunit 3
Nd4L	NADH Dehydrogenase Subunit 4L
Hk2	Hexokinase 2
Pdk1	Pyruvate dehydrogenase kinase 1
PFKM	Phosphofructokinase-muscle
LDs	Lipid droplets

Supplementary Information

The online version contains supplementary material available at https://doi.org/10.1186/s12951-025-03717-z.

Additional file1

Acknowledgements
All schematic diagrams were created with BioRender.com. Graphical abstract was created in BioRender. Guo, J. (2025) https://BioRender.com/l24t736. Figure 6 A was created in BioRender. Guo, J. (2025) https://BioRender.com/e15g136. Figure 9 A was created in BioRender. Guo, J. (2025) https://BioRender.com/i58t172.

Author contributions
J.G. and L.Q. designed and supervised the study. Q.Q., X.Y. and Z.Z. performed the experiments. X.Z., W.G. and J.M. collected and analyzed the data. J.G., Q.Q. and X.Y. wrote the manuscript. J.G., L.Q. and N.A. provided financial support and revised manuscript. The authors read and approved the final manuscript.

Funding
This work was supported by the National Natural Science Foundation of China (81900992, 81870752, 82470970), the China Postdoctoral Science Foundation (2021MD703905), and the Natural Science Foundation of Liaoning Province (2023-BS-097).

Data availability
The data that support the findings of this study are available from the corresponding authors on reasonable request.

Declarations

Ethics approval
Animal studies were performed in accordance with the guidelines approved by the Institutional Animal Care and Use Committee of China Medical University (CMU2023680, CMU20241480).

Consent for publication
Not applicable.

Competing of interests
The authors declare no competing interests.

Author details
[1]Department of Endodontics, School and Hospital of Stomatology, Liaoning Provincial Key Laboratory of Oral Diseases, China Medical University, Shenyang 110001, China
[2]Department of Orthodontics, School and Hospital of Stomatology, Liaoning Provincial Key Laboratory of Oral Diseases, China Medical University, Shenyang 110001, China

Received: 21 April 2025 / Accepted: 16 September 2025
Published online: 10 October 2025

References

1. Bartold PM. Lifestyle and periodontitis: The emergence of personalized periodontics. Periodontol 2000. 2018;78:7–11.
2. Reginster JY, Burlet N. Osteoporosis: A still increasing prevalence. Bone. 2006;38:S4-9.
3. Huang YF, Chang CT, Liu SP, Muo CH, Tsai CH, Hong HH, et al. The impact of oral hygiene maintenance on the association between periodontitis and osteoporosis: A nationwide population-based cross sectional study. Medicine (Baltimore). 2016;95:e2348.
4. Anbinder AL, Moraes RM, Lima GMG, Oliveira FE, Campos DRC, Rossoni RD, et al. Periodontal disease exacerbates systemic ovariectomy-induced bone loss in mice. Bone. 2016;83:241–7.
5. Wang N, Zheng L, Qian J, Wang M, Li L, Huang Y, et al. Salivary microbiota of periodontitis aggravates bone loss in ovariectomized rats. Front Cell Infect Microbiol. 2022;12:983608.
6. Zhang ZY, Xie MR, Liu Y, Li YX, Wu K, Ding YM. Effect of periodontal pathogens on total bone volume fraction: A phenotypic study. Curr Med Sci. 2020;40:753–60.
7. Amano A, Chen C, Honma K, Li C, Settem RP, Sharma A. Genetic characteristics and pathogenic mechanisms of periodontal pathogens. Adv Dent Res. 2014;26:15–22.
8. Luo X, Wang Y, Ning T, Lei Q, Cui H, Zou X, et al. Outer membrane vesicles of *Porphyromonas gingivalis* impede bone regeneration by inducing ferroptosis via the Hippo-YAP signaling pathway. J Nanobiotechnology. 2025;23:358.
9. Seyama M, Yoshida K, Yoshida K, Fujiwara N, Ono K, Eguchi T, et al. Outer membrane vesicles of *Porphyromonas gingivalis* attenuate insulin sensitivity by delivering gingipains to the liver. Biochimica et Biophysica Acta (BBA). 2020;1866:165731.
10. Toyofuku M, Schild S, Kaparakis-Liaskos M, Eberl L. Composition and functions of bacterial membrane vesicles. Nat Rev Microbiol. 2023;21:415–30.
11. Tulkens J, De Wever O, Hendrix A. Analyzing bacterial extracellular vesicles in human body fluids by orthogonal biophysical separation and biochemical characterization. Nat Protoc. 2020;15:40–67.
12. Han EC, Choi SY, Lee Y, Park JW, Hong SH, Lee HJ. Extracellular RNAs in periodontopathogenic outer membrane vesicles promote TNF-alpha production in human macrophages and cross the blood-brain barrier in mice. FASEB J. 2019;33:13412–22.
13. Ha JY, Choi SY, Lee JH, Hong SH, Lee HJ. Delivery of periodontopathogenic extracellular vesicles to brain monocytes and microglial IL-6 promotion by RNA cargo. Front Mol Biosci. 2020;7:596366.
14. Kim HY, Song MK, Gho YS, Kim HH, Choi BK. Extracellular vesicles derived from the periodontal pathogen *Filifactor alocis* induce systemic bone loss through Toll-like receptor 2. J Extracell Vesicles. 2021;10:e12157.
15. Choi JY. Healthy bone tissue homeostasis. Exp Mol Med. 2020;52:1165.
16. Ponzetti M, Rucci N. Osteoblast differentiation and signaling: Established concepts and emerging topics. Int J Mol Sci. 2021;22(13):6651.
17. Wu J, Hu M, Jiang H, Ma J, Xie C, Zhang Z, et al. Endothelial cell-derived lactate triggers bone mesenchymal stem cell histone lactylation to attenuate osteoporosis. Adv Sci (Weinh). 2023;10:e2301300.
18. Yang Z, Zhang XW, Zhuo FF, Liu TT, Luo QW, Zheng YZ, et al. Allosteric activation of transglutaminase 2 via inducing an "open" conformation for osteoblast differentiation. Adv Sci (Weinh). 2023;10:e2206533.
19. Zou W, Chen Q, Slone J, Yang L, Lou X, Diao J, et al. Nanoscopic quantification of sub-mitochondrial morphology, mitophagy and mitochondrial dynamics in living cells derived from patients with mitochondrial diseases. J Nanobiotechnology. 2021;19:136.
20. Buck MD, O'Sullivan D, Klein Geltink RI, Curtis JD, Chang CH, Sanin DE, et al. Mitochondrial dynamics controls T cell fate through metabolic programming. Cell. 2016;166:63–76.
21. Liu Y, Wu Z, Li Y, Chen Y, Zhao X, Wu M, et al. Metabolic reprogramming and interventions in angiogenesis. J Adv Res. 2024;70:323–38.
22. Niemeier A, Niedzielska D, Secer R, Schilling A, Merkel M, Enrich C, et al. Uptake of postprandial lipoproteins into bone in vivo: Impact on osteoblast function. Bone. 2008;43:230–7.
23. Frey JL, Li Z, Ellis JM, Zhang Q, Farber CR, Aja S, et al. Wnt-Lrp5 signaling regulates fatty acid metabolism in the osteoblast. Mol Cell Biol. 2015;35:1979–91.

24. Kushwaha P, Wolfgang MJ, Riddle RC. Fatty acid metabolism by the osteoblast. Bone. 2018;115:8–14.
25. Haynie KR, Vandanmagsar B, Wicks SE, Zhang J, Mynatt RL. Inhibition of carnitine palymitoyltransferase1b induces cardiac hypertrophy and mortality in mice. Diabetes Obes Metab. 2014;16:757–60.
26. Wolfgang MJ, Lane MD. Control of energy homeostasis: Role of enzymes and intermediates of fatty acid metabolism in the central nervous system. Annu Rev Nutr. 2006;26:23–44.
27. Kim SP, Li Z, Zoch ML, Frey JL, Bowman CE, Kushwaha P, et al. Fatty acid oxidation by the osteoblast is required for normal bone acquisition in a sex- and diet-dependent manner. JCI Insight. 2017.
28. Antezack A, Etchecopar-Etchart D, La Scola B, Monnet-Corti V. New putative periodontopathogens and periodontal health-associated species: A systematic review and meta-analysis. J Periodontal Res. 2023;58:893–906.
29. Lombardo Bedran TB, Marcantonio RA, Spin Neto R, Alves Mayer MP, Grenier D, Spolidorio LC, et al. *Porphyromonas endodontalis* in chronic periodontitis: A clinical and microbiological cross-sectional study. J Oral Microbiol. 2012;4(1):10123.
30. Arifin WN, Zahiruddin WM. Sample size calculation in animal studies using resource equation approach. Malays J Med Sci. 2017;24:101–5.
31. Deng DK, Zhang JJ, Gan D, Zou JK, Wu RX, Tian Y, et al. Roles of extracellular vesicles in periodontal homeostasis and their therapeutic potential. J Nanobiotechnology. 2022;20:545.
32. Kim SW, Park SB, Im SP, Lee JS, Jung JW, Gong TW, Lazarte JMS, Kim J, Seo JS, Kim JH, Song JW, Jung HS, Kim GJ, Lee YJ, Lim SK, Jung TS. Outer membrane vesicles from beta-lactam-resistant *Escherichia coli* enable the survival of beta-lactam-susceptible *E. coli* in the presence of beta-lactam antibiotics. Sci Rep. 2018;8:5402.
33. Aldick T, Bielaszewska M, Uhlin BE, Humpf HU, Wai SN, Karch H. Vesicular stabilization and activity augmentation of enterohaemorrhagic *Escherichia coli* haemolysin. Mol Microbiol. 2009;71(6):1496–508.
34. Zingl FG, Thapa HB, Scharf M, Kohl P, Muller AM, Schild S. Outer membrane vesicles of *Vibrio cholerae* protect and deliver active cholera toxin to host cells via porin-dependent uptake. MBio. 2021;12:e0053421.
35. Alves NJ, Turner KB, Medintz IL, Walper SA. Protecting enzymatic function through directed packaging into bacterial outer membrane vesicles. Sci Rep. 2016;6:24866.
36. Rompikuntal PK, Vdovikova S, Duperthuy M, Johnson TL, Ahlund M, Lundmark R, et al. Outer membrane vesicle-mediated export of processed PrtV protease from *Vibrio cholerae*. PLoS ONE. 2015;10:e0134098.
37. Li F, Ma C, Lei S, Pan Y, Lin L, Pan C, et al. Gingipains may be one of the key virulence factors of *Porphyromonas gingivalis* to impair cognition and enhance blood-brain barrier permeability: An animal study. J Clin Periodontol. 2024;51:818–39.
38. Liu Y, Cui B, Zhang P, Xiao S, Duan D, Ding Y. Polymicrobial infection induces adipose tissue dysfunction via gingival extracellular vesicles. J Dent Res. 2024;103:187–96.
39. Reyes L, Getachew H, Dunn WA, Progulske-Fox A. *Porphyromonas gingivalis* W83 traffics via ICAM1 in microvascular endothelial cells and alters capillary organization in vivo. J Oral Microbiol. 2020;12:1742528.
40. Niu C, Huang J, Wei L, Wang J, Ran S. Proinflammatory effect of membrane vesicles derived from enterococcus faecalis at neutral and alkaline pH. J Endod. 2024;50(1602–11):e10.
41. Su X, Wang H, Li Q, Chen Z. Extracellular vesicles: A review of their therapeutic potentials, sources, biodistribution, and administration routes. Int J Nanomedicine. 2025;20:3175–99.
42. Zhou X, Li Z, Sun W, Yang G, Xing C, Yuan L. Delivery efficacy differences of intravenous and intraperitoneal injection of exosomes: Perspectives from tracking dye labeled and miRNA encapsulated exosomes. Curr Drug Deliv. 2020;17:186–94.
43. Fleetwood AJ, Lee MKS, Singleton W, Achuthan A, Lee MC, O'Brien-Simpson NM, et al. Metabolic remodeling, inflammasome activation, and pyroptosis in macrophages stimulated by *Porphyromonas gingivalis* and its outer membrane vesicles. Front Cell Infect Microbiol. 2017;7:351.
44. Chen G, Sun Q, Cai Q, Zhou H. Outer membrane vesicles from *Fusobacterium nucleatum* switch M0-like macrophages toward the M1 phenotype to destroy periodontal tissues in mice. Front Microbiol. 2022;13:815638.
45. Luo S, Xu T, Zheng Q, Jiang A, Zhao J, Ying Y, et al. Mitochondria: An emerging unavoidable link in the pathogenesis of periodontitis caused by *porphyromonas gingivalis*. Int J Mol Sci. 2024;25(2):737.
46. Chen X, He Q, Zhai Q, Tang H, Li D, Zhu X, et al. Adaptive nanoparticle-mediated modulation of mitochondrial homeostasis and inflammation to enhance infected bone defect healing. ACS Nano. 2023;17:22960–78.
47. Araiso Y, Tsutsumi A, Qiu J, Imai K, Shiota T, Song J, et al. Structure of the mitochondrial import gate reveals distinct preprotein paths. Nature. 2019;575:395–401.
48. Galloway CA, Yoon Y. Mitochondrial morphology in metabolic diseases. Antioxid Redox Signal. 2013;19:415–30.
49. Yu Y, Peng XD, Qian XJ, Zhang KM, Huang X, Chen YH, et al. Fis1 phosphorylation by Met promotes mitochondrial fission and hepatocellular carcinoma metastasis. Signal Transduct Target Ther. 2021;6:401.
50. Navaratnarajah T, Anand R, Reichert AS, Distelmaier F. The relevance of mitochondrial morphology for human disease. Int J Biochem Cell Biol. 2021;134:105951.
51. Kleele T, Rey T, Winter J, Zaganelli S, Mahecic D, Perreten Lambert H, et al. Distinct fission signatures predict mitochondrial degradation or biogenesis. Nature. 2021;593:435–9.
52. Xu T, Dong Q, Luo Y, Liu Y, Gao L, Pan Y, et al. *Porphyromonas gingivalis* infection promotes mitochondrial dysfunction through Drp1-dependent mitochondrial fission in endothelial cells. Int J Oral Sci. 2021;13:28.
53. Liu M, Fan Y, Li D, Han B, Meng Y, Chen F, et al. Ferroptosis inducer erastin sensitizes NSCLC cells to celastrol through activation of the ROS-mitochondrial fission-mitophagy axis. Mol Oncol. 2021;15:2084–105.
54. Green DE. Mitochondria–structure, function, and replication. N Engl J Med. 1983;309:182–3.
55. Escoll P, Song OR, Viana F, Steiner B, Lagache T, Olivo-Marin JC, et al. *Legionella pneumophila* modulates mitochondrial dynamics to trigger metabolic repurposing of infected macrophages. Cell Host Microbe. 2017;22(302–16):e7.
56. Lee WC, Guntur AR, Long F, Rosen CJ. Energy metabolism of the osteoblast: Implications for osteoporosis. Endocr Rev. 2017;38:255–66.
57. Wang Y, Deng P, Liu Y, Wu Y, Chen Y, Guo Y, et al. Alpha-ketoglutarate ameliorates age-related osteoporosis via regulating histone methylations. Nat Commun. 2020;11:5596.
58. Nandy A, Helderman RCM, Thapa S, Jayapalan S, Richards A, Narayani N, et al. Lipolysis supports bone formation by providing osteoblasts with endogenous fatty acid substrates to maintain bioenergetic status. Bone Res. 2023;11:62.
59. Tan W, Wang Y, Cheng S, Liu Z, Xie M, Song L, et al. AdipoRon ameliorates the progression of heart failure with preserved ejection fraction via mitigating lipid accumulation and fibrosis. J Adv Res. 2025;68:299–315.
60. Yan J, Herzog JW, Tsang K, Brennan CA, Bower MA, Garrett WS, et al. Gut microbiota induce IGF-1 and promote bone formation and growth. Proc Natl Acad Sci U S A. 2016;113:E7554–63.
61. Vanek C, Connor WE. Do n-3 fatty acids prevent osteoporosis? Am J Clin Nutr. 2007;85:647–8.
62. Miranda M, Pino AM, Fuenzalida K, Rosen CJ, Seitz G, Rodriguez JP. Characterization of fatty acid composition in bone marrow fluid from postmenopausal women: Modification after hip fracture. J Cell Biochem. 2016;117:2370–6.
63. Guo Y, Zhang Z, Wen Z, Kang X, Wang D, Zhang L, et al. Mitochondrial SIRT2-mediated CPT2 deacetylation prevents diabetic cardiomyopathy by impeding cardiac fatty acid oxidation. Int J Biol Sci. 2025;21:725–44.
64. Li J, Qi J, Tang Y, Liu H, Zhou K, Dai Z, et al. A nanodrug system overexpressed circRNA_0001805 alleviates nonalcoholic fatty liver disease via miR-106a-5p/miR-320a and ABCA1/CPT1 axis. J Nanobiotechnology. 2021;19:363.
65. Ngo J, Choi DW, Stanley IA, Stiles L, Molina AJA, Chen PH, et al. Mitochondrial morphology controls fatty acid utilization by changing CPT1 sensitivity to malonyl-CoA. EMBO J. 2023;42:e111901.
66. Guo X, Wang A, Wang W, Wang Y, Chen H, Liu X, et al. HRD1 inhibits fatty acid oxidation and tumorigenesis by ubiquitinating CPT2 in triple-negative breast cancer. Mol Oncol. 2021;15:642–56.
67. Wei J, Yuan Y, Chen L, Xu Y, Zhang Y, Wang Y, et al. ER-associated ubiquitin ligase HRD1 programs liver metabolism by targeting multiple metabolic enzymes. Nat Commun. 2018;9:3659.
68. Gu Q, Yang H, Shi Q. Macrophages and bone inflammation. J Orthop Translat. 2017;10:86–93.
69. Alvarez G, Arredondo A, Isabal S, Teughels W, Laleman I, Contreras MJ, et al. Association of nine pathobionts with periodontitis in four South American and European countries. J Oral Microbiol. 2023;15:2188630.
70. Cao H, Qi Z, Jiang H, Zhao J, Liu Z, Tang Z. Detection of *Porphyromonas endodontalis*, *Porphyromonas gingivalis* and *Prevotella intermedia* in primary endodontic infections in a Chinese population. Int Endod J. 2012;45:773–81.

71. Bordagaray MJ, Fernandez A, Garrido M, Astorga J, Hoare A, Hernandez M. Systemic and extraradicular bacterial translocation in apical periodontitis. Front Cell Infect Microbiol. 2021;11:649925.
72. Rosen G, Shoshani M, Naor R, Sela MN. The purification and characterization of an 88-kDa *Porphyromonas endodontalis* 35406 protease. Oral Microbiol Immunol. 2001;16:326–31.
73. Dominy SS, Lynch C, Ermini F, Benedyk M, Marczyk A, Konradi A, et al. *Porphyromonas gingivalis* in Alzheimer's disease brains: Evidence for disease causation and treatment with small-molecule inhibitors. Sci Adv. 2019;5:eaau3333.
74. Chow YC, Yam HC, Gunasekaran B, Lai WY, Wo WY, Agarwal T, et al. Implications of *Porphyromonas gingivalis* peptidyl arginine deiminase and gingipain R in human health and diseases. Front Cell Infect Microbiol. 2022;12:987683.

Publisher's Note

Springer Nature remains neutral with regard to jurisdictional claims in published maps and institutional affiliations.